

Exsolution Synthesis of Nanocomposite Perovskites with Tunable Electrical and Magnetic Properties

Jiayue Wang, Komal Syed, Shuai Ning, Iradwikanari Waluyo, Adrian Hunt, Ethan J. Crumlin, Alexander K. Opitz, Caroline A. Ross, William J. Bowman, and Bilge Yildiz*

Nanostructured functional oxides play an important role in enabling clean energy technologies and novel memory and processor devices. Using thin-film $\text{La}_{0.6}\text{Sr}_{0.4}\text{FeO}_3$ (LSF) as a model system, the novel utility of exsolution in fabricating self-assembled metal oxide nanocomposites with tunable functionalities is shown. Exsolution triggers the formation of metallic iron (Fe^0) nanoparticles, Ruddlesden–Popper domains, and nm-scale percolated Fe-deficient channels in LSF. Combining multimodal characterization with numerical modeling, the chemical, magnetic, and electrical properties of the exsolution-synthesized nanocomposite at different stages of Fe^0 exsolution as well as during redox cycling are assessed. After exsolution, the electronic conductivity of the nanocomposite LSF increased by more than two orders of magnitude. Based on numerical analysis representing all the constituents, it is expected that this increase in conductivity originates mainly from the Fe-deficient percolating channels formed during exsolution. Moreover, the exsolved nanocomposite is redox-active even at moderate temperatures. Such redox capabilities can enable dynamic control of the nanocomposite functionality by tailoring the oxygen non-stoichiometry. This concept is demonstrated with a continuous modulation of magnetization between 0 and 110 emu cm^{-3} . These findings point out that exsolution may serve as a platform for scalable fabrication of complex metal oxide nanocomposites for electrochemical and electronic applications.

has been used to increase the electronic conductivity in solid oxide cells (SOCs),^[12] as well as to improve the uniformity in resistive switching.^[13–15] It is desirable to develop scalable synthesis methods that can precisely control the chemical and structural features, and thereby the functional properties of the nanocomposites.^[3,16]

Exsolution is a partial decomposition process where metallic nanoparticles are precipitated out of the host metal-oxide matrix upon thermal or electrochemical reduction.^[17–20] Compared to nanoparticles prepared by deposition or impregnation,^[21] the exsolved nanoparticles have three unique advantages: First, exsolution can generate nanoparticles both on the surface^[17–20,22] and in the interior.^[15,22–25] Such flexibility makes exsolution a powerful method to fabricate nanostructures at specific, otherwise inaccessible locations in the devices. Second, the exsolved nanoparticles can either reintegrate into the host oxide,^[19,26–28] or reversibly oxidize at their initially exsolved locations.^[24,29,30] This reversible redox ability opens up the possibility to switch functional properties of the materials during operation.^[19,30,31] Finally, for catalytic applications, the anchored structure^[18] of the exsolved nanoparticles on the surface makes them highly stable against particle coarsening and aging.^[29]

1. Introduction

Nanocomposite oxides^[1–4] have been considered as a promising platform to optimize the electronic,^[5] mass/ion transport,^[6–9] magnetic,^[10] and catalytic^[11] properties of the materials. For example, integration of metallic phases into the oxide matrix

J. Wang, B. Yildiz
Department of Nuclear Science and Engineering
Massachusetts Institute of Technology
Cambridge, MA 02139, USA
E-mail: byildiz@mit.edu

K. Syed, W. J. Bowman
Department of Materials Science and Engineering
University of California
Irvine, CA 92617, USA


S. Ning, C. A. Ross, B. Yildiz
Department of Materials Science and Engineering
Massachusetts Institute of Technology
Cambridge, MA 02139, USA

S. Ning
School of Materials Science and Engineering
Nankai University
Tianjin 300350, P. R. China

I. Waluyo, A. Hunt
National Synchrotron Light Source II
Brookhaven National Laboratory
Upton, NY 11973, USA

E. J. Crumlin
Advanced Light Source, Lawrence Berkeley National Laboratory
Berkeley, CA 94720, USA

A. K. Opitz
Institute of Chemical Technologies and Analytics
TU Wien
Vienna 1060, Austria

 The ORCID identification number(s) for the author(s) of this article can be found under <https://doi.org/10.1002/adfm.202108005>.

DOI: 10.1002/adfm.202108005

While exsolution has been extensively employed to enhance surface catalytic properties,^[19,23,30,32,33] its potential to modulate bulk properties remains open. In fact, given that the original application has been in catalysis, bulk exsolution has been considered as an undesirable process.^[27,28] Herein, we propose that exsolution can provide new opportunities in synthesizing functional nanocomposite oxides with customizable structures and functionalities. First, since exsolution is a partial decomposition process, it can generate multiple phases^[34] and different types of lattice defects^[35–37] in the host oxides. Such defects are paramount for a wide range of electrical, optical, and magnetic properties,^[38–40] which provides a tuning knob to tailor materials' functionality by controlling the extent of exsolution. Second, since exsolution can be implemented to a wide class of materials and does not require a delicate synthetic platform, it can act as a scalable and practical approach to synthesize self-assembled functional nanocomposites. For rational synthesis of exsolved nanocomposites, one has to carefully control the exsolution parameters through the underlying mechanisms. To date, it still remains unclear as to how exsolution affects the structure, chemistry, and properties in the bulk of the host oxide.

In this work, we chose single-phase thin-film $\text{La}_{0.6}\text{Sr}_{0.4}\text{FeO}_3$ (LSF) as a model perovskite oxide to systematically investigate the bulk exsolution process. LSF is a suitable model system due to its well-studied bulk defect chemistry,^[41] and its broad applications in chemical looping,^[42] SOCs,^[30] and magnetic nanostructure formation.^[43] Moreover, thin-film LSF has also been employed as model systems to investigate surface exsolution in previous studies.^[30,37,44] We showed that exsolution in such oxide thin films generates not only metal nanoparticles (as in prior work), but also more complex nanostructures with implications for the thin-film properties; including crystalline Ruddlesden-Popper (RP) domains and percolated Fe-deficient nm-scale channels. These phenomena, to the best of our knowledge, are reported for the first time in LSF. While previous studies mainly focused on the exsolved metal nanoparticles, in this study we provide novel findings that the exsolution-induced extended defects can also be critical in determining the final functionality and property of the evolving composite material. Combining multimodal experiments with numerical simulations, we demonstrated that besides the exsolved Fe^0 nanoparticles, the Fe-deficient percolating channels formed during exsolution can increase the electronic conductivity of the nanocomposite LSF by more than two orders of magnitude.

Furthermore, we achieved a multi-state control of the exsolved nanocomposite and the quantification of that state reliably. For this, one needs to control the exsolution extent in the material and quantify its properties without altering the exsolution state. This task, however, is not trivial. In our previous study,^[37] we have shown that the surface exsolved metal nanoparticle can be quickly re-oxidized into metal oxides upon air exposure. Moreover, we have shown that the nanoparticle exsolution in thin-film samples would not induce noticeable changes in the ex situ XRD diffraction.^[37] Therefore, it is very challenging, if not impossible, to accurately measure the exsolution states and the corresponding materials properties' in the exsolved nanocomposites using ex situ characterizations. To address this challenge, here we employed state-of-the-art near

ambient pressure X-ray photoelectron spectroscopy (NAP-XPS) measurements to synthesize and characterize exsolved nanocomposite at different exsolution extents and at different stages of re-oxidation. Using this method, we unambiguously demonstrate that one can realize a multi-stage control of the electrical conductivity (by more than 2 orders of magnitude), and the magnetization (between 0 and 110 emu cm^{-3}) of the nanocomposite LSF by controllably tailoring the oxygen non-stoichiometry and the exsolution extent. These findings not only extend the mechanistic understanding of the bulk exsolution process, but also provide motivation to nano-engineer oxide thin films for novel and tunable properties via the exsolution route.

2. Results and Discussion

2.1. Structure and Chemistry of the Exsolved Nanocomposite LSF

To begin with, we demonstrate that bulk exsolution can transform a single-phase perovskite oxide into a metal/oxide nanocomposite (schematically shown in **Figure 1a**). In particular, we will examine the resulting heterogeneous chemical, atomic and electronic structure of the exsolved nanocomposite, as this has significant implications for the properties of interest. As shown in **Figure 1b**, 120 nm thick polycrystalline LSF films were deposited onto MgO (001) single crystal substrates using pulsed laser deposition (PLD) (for film growth details see Experimental Section). θ -2 θ X-ray diffraction (XRD) confirmed the dominant (001) texture of the polycrystalline LSF film, while a small amount of (011) contribution can also be observed (Note S1, Supporting Information). Scanning transmission electron microscopy (STEM) high-angle annular dark-field (HAADF) imaging was employed to demonstrate the cross-sectional structure of the LSF films before and after exsolution. The as-prepared LSF specimen shows a columnar structure with little contrast other than vertical striations. After reducing the sample at 400 °C in 0.5 Torr flowing H_2 , a variety of nanostructures with varying Z-contrast can be observed throughout the exsolved LSF film (**Figure 1b**). As shown in **Figure 1c**, nanoparticles can be clearly seen both on the surface and in the bulk of the exsolved sample. In accordance with the STEM images, the surface morphology of the LSF film also evolved during the exsolution process. After exsolution, small particles with a mean radius of ca. 8 nm appeared on the surface. Representative atomic force microscopy (AFM) and scanning electron microscopy (SEM) images are presented in the Note S1, Supporting Information.

Furthermore, we have also observed numerous channel-like features in the exsolved LSF film, featured by the threading dark stripes in **Figure 1d-top**. The nanoparticle precipitates are typically located along these channels. As highlighted by the white dashed lines in **Figure 1d-bottom**, these channels form long-range connectivity (i.e., percolation)^[41] across the entire exsolved sample. Since such percolating channels did not exist in the as-prepared sample (**Figure 1b** and Note S1, Supporting Information), they must be formed during the exsolution process together with the nanoparticles. The dark contrast of the percolating channels in the HAADF images suggest that they may contain considerable structural disorder.^[42] In addition,

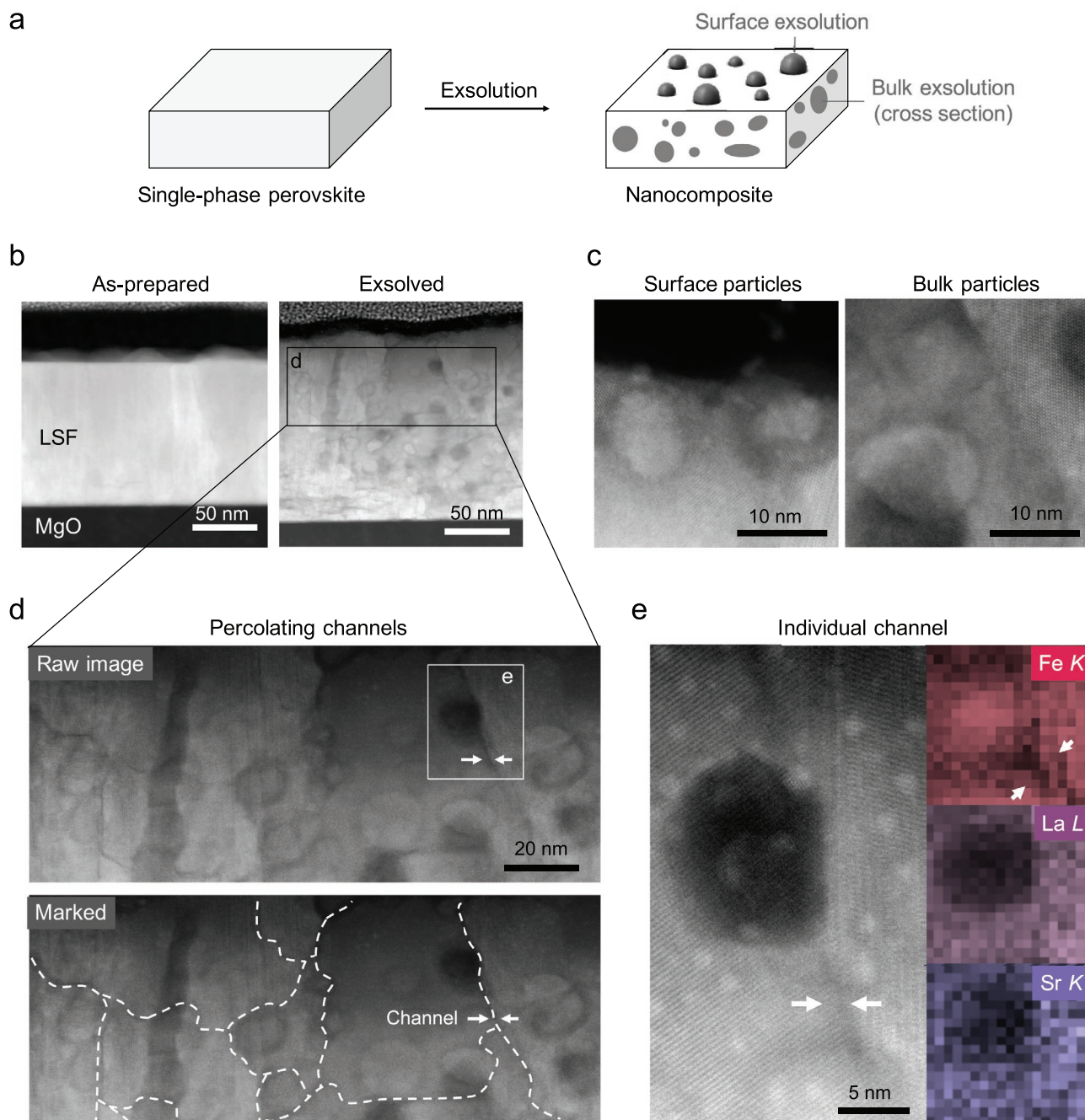


Figure 1. Exsolution nanocomposite. a) Simplified sketch of synthesizing metal oxide nanocomposite via exsolution. b) Cross-sectional scanning HAADF images of the LSF film before and after Fe^0 exsolution. c) High-resolution HAADF images showing the nanoparticles on the surface and in the bulk of the exsolved LSF film. d) Magnified HAADF image from the region highlighted in (b) showing the percolating channels in the exsolved LSF film. The dashed lines marked the location of the channels. e) High magnification HAADF and the corresponding EDX chemical mapping showing an individual channel. Note the channel is depleted in Fe. Plot (e) was collected from the region highlighted in (d) with a solid box.

these percolating channels are depleted in Fe as seen by energy dispersive spectroscopy (EDX) mapping (Figure 1e and Note S2, Supporting Information). We are aware that similar percolating channels have also been observed in partially decomposed cobalt-based perovskites^[34] and lithium-excess cathode materials,^[43] and were identified as the fast cation migration channels in those systems. In analogy to those systems, the percolating

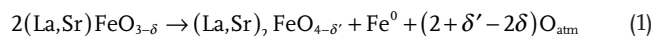
channels in the exsolved LSF may act as the diffusion pathways that connect to regions where Fe has been exsolved from. This may also explain why the exsolved nanoparticles are preferentially located along these channels. It should also be noted that while each percolating channel appeared as a 1D line defect in the projected HAADF images (Figure 1d,e), they can be 2D structures in the interior of the film. In the following

paragraphs, we will demonstrate that many of these channels are phase boundaries. At this point we cannot identify precisely the atomic and chemical state of these Fe-deficient percolating channels. For the remaining of the paper, we will refer to these features as “channels” for simplicity. The formation of such percolating structures is important to note because this can lead to significant changes in the macroscopic transport properties of the oxide film, arising from the local properties of these structures being different from those of the original material.^[43–45] In this study, we will demonstrate that the exsolution-induced percolating channels can lead to an electrical conductivity increase by more than two orders of magnitude compared to the original LSF films (to be discussed later).

A detailed phase analysis of the exsolved nanocomposite LSF is presented in Figure 2. Unlike the as-prepared LSF film that has a homogeneous bulk chemistry (Note S3, Supporting Information), the exsolved LSF exhibited considerable chemical inhomogeneity. As shown in Figure 2a,b and Figure S8, Supporting Information, the nanoparticles both at the surface and in the bulk are enriched in Fe while depleted in La and Sr. Zoom-in views of these Fe-enriched nanoparticles are presented in Figure 2c,e. With the aid of fast Fourier transformation (FFT) analysis (Figure 2d,f), we assign the bulk nanoparticles to be α -Fe (PDF#00-006-0696).^[46] Meanwhile, surface nanoparticles could be either Fe₃O₄ (PDF#01-071-6336)^[47] or γ -Fe₂O₃ (PDF# 00-039-1346).^[48] As both iron oxide phases adopt similar inverse spinel structures,^[49,50] we cannot unambiguously distinguish between them in this work. Nevertheless, the observation of iron oxides on the surface clearly indicates that the surface Fe⁰ particles became oxidized during sample transfer for TEM analysis. In agreement with our findings, re-oxidation of the surface exsolved metal nanoparticles into metal oxides has also been reported in previous studies.^[30,51] On the other hand, the α -Fe particles embedded in the bulk are protected from oxidation upon air exposure of the sample surface.

The fuzzy layer around the exsolved nanoparticles reflects the phase boundary. As labeled in Figure 2c,e, we identified two distinct phases adjacent to the exsolved nanoparticles. Based on the interatomic lattice spacing revealed by the high-resolution images (Figure 2d,f), we assigned these two phases to be perovskite-type (La,Sr)FeO₃ (PDF#04-007-6521)^[52] and RP-type (La,Sr)₂FeO₄ (PDF#01-082-8811),^[53] and denoted as LSC₁₁₃ and LSC₂₁₄ respectively. These observations indicate that many of Fe-deficient percolating channels observed in Figure 1d,e are phase boundaries between the LSF₁₁₃ and LSF₂₁₄ domains. Nevertheless, as shown in the Note S2, Supporting Information, we also find a few percolating channels are located within a single phase.

Therefore, the Fe⁰ nanoparticle exsolution both at the surface and in the bulk is correlated with the formation of the RP phase. This is consistent with the bulk phase decomposition of LSF into iron metal and RP phase under reducing conditions.^[54,55] As such, we can describe the nanocomposite formation in LSF with the following reaction:



where O_{atm} denotes a gas-phase oxygen, which can be present in the form of different molecules (such as H₂O or CO₂) depending on the reducing agent. Meanwhile, δ and δ' denote

oxygen nonstoichiometry in the perovskite and RP phase, respectively. We are aware that cation vacancies can also exist in both phases. Nevertheless, since the purpose of Equation (1) is to provide a general description of the exsolution process, we use the current format for simplicity. It should be also noted that we did not observe discernible reflections from the α -Fe and RP phases in the nanocomposite LSF with $\theta - 2\theta$ XRD (Note S1, Supporting Information), likely due to the small crystalline volume fraction of both phases. Therefore, we expect the perovskite LSF remains as the dominant phase (matrix) even after Fe⁰ exsolution. The preservation of the perovskite-type structure indicates a good structural stability of the LSF lattice during Fe⁰ exsolution under the conditions of these experiments.

Finally, we employed ex situ partial fluorescence-yield X-ray absorption spectroscopy (PFY-XAS) to demonstrate the evolution of bulk chemistry upon nanocomposite formation. For La M₅-edge (Figure 2g), we did not observe noticeable changes in the main peak, indicating a constant oxidation state of La during exsolution. On the other hand, the increased pre-edge intensity at ca. 707 eV in Fe L₃-edge after exsolution (Figure 2h) suggests the presence of metallic iron (Fe⁰) in the nanocomposite LSF.^[56] Note the Fe⁰ feature in the Fe L₃-edge agrees well with the α -Fe particles observed by STEM characterization (Figure 2e,f). Regarding the O K-edge (Figure 2i), the pre-edge feature A in the as-prepared LSF corresponds to the transition from O 1s to the ligand hole *L* in the 3d⁵*L* configuration.^[57,58] The pre-edge peak vanished after exsolution, indicating a filling of the ligand band, which corresponds to a reduction of the LSF film.^[57] In agreement with the pre-edge evolution in the O K-edge, lattice chemical expansion^[59,60] has also been observed after exsolution (Note S1, Supporting Information), which confirms the increased oxygen vacancy concentration in the nanocomposite LSF. The two peaks between 529 and 532 eV (feature B) in the as-prepared LSF have been assigned to the unoccupied *t*_{2g}↓ and *e*_g↓ states, respectively.^[57,58] The variation of these absorption features during exsolution may indicate a change in covalency.^[57] Finally, a new feature emerged at around 532.5 eV (feature C) after exsolution. Since feature C did not exist in the mildly reduced LSF film (Note S4, Supporting Information), it should be related to the new phase(s) or lattice defect(s) that are formed in exsolution. Accordingly, the peak position of feature C agrees with the La/Sr–O hybridization of La₂O₃,^[61] SrO,^[61] and RP phase oxides,^[34,62,63] which are all likely decomposition products of LSF during exsolution.^[19,64–66] Therefore, while the nanocomposite LSF is mainly composed of the perovskite matrix, it exhibits completely different electronic structures from the perovskite LSF. As indicated earlier, this will have implications for the resulting electronic and magnetic properties of the exsolved nanocomposite with respect to the initial LSF.

2.2. Enhanced Electrical Conductivity from In Situ Fe⁰ Exsolution

Having demonstrated that Fe⁰ exsolution can transform the single-phase perovskite LSF into a triple-phase nanocomposite, we now turn to its impact on the functionalities of the material. The experimental setup is schematically shown in Figure 3a. As illustrated, NAP-XPS and in-plane electrical conductivity measurements were performed simultaneously to monitor the

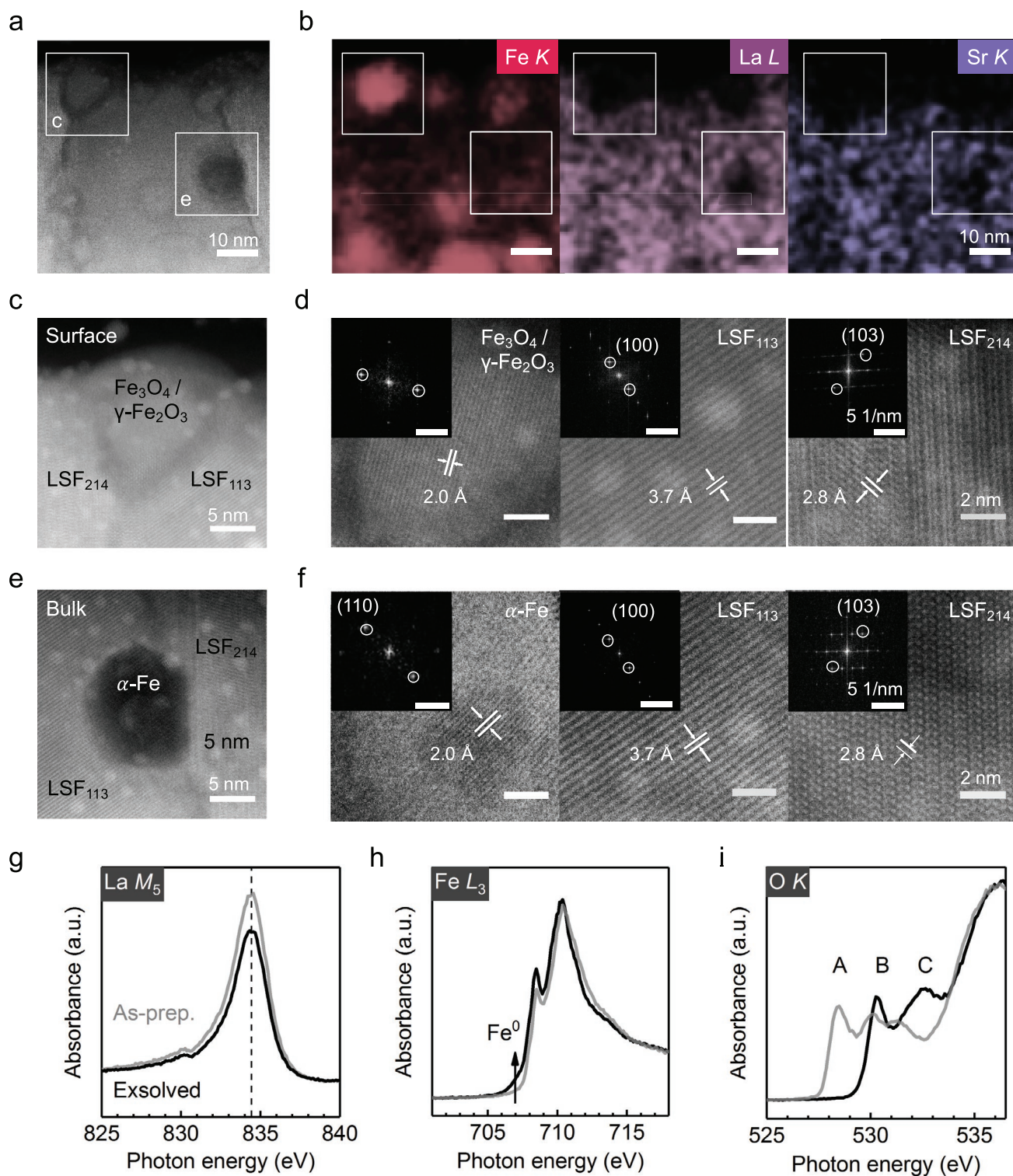


Figure 2. Atomic structure and chemical nature of the nanocomposite LSF. a) Low magnification HAADF and b) the corresponding EDX chemical mapping showing the chemical inhomogeneity of the exsolved LSF. High-resolution HAADF images of the c) surface and e) bulk nanocomposite, which are acquired from the regions highlighted in (a,b) with the solid boxes. d,f) High-resolution images (scale bars: 2nm) showing the lattice fringes of the three different phases in (c, e) with the inset diffractogram from FFT (scale bars: 5 1/nm). The labeled lattice spacing corresponds to the circled FFT patterns. LSF₁₁₃ and LSF₂₁₄ denote the perovskite phase and the RP phase, respectively. g) La M₅-edge, h) Fe L₃-edge, and i) O K-edge PFY-XAS measurements revealing the macroscopically averaged bulk chemistry and electronic structure of the LSF film before (gray lines) and after (black lines) exsolution.

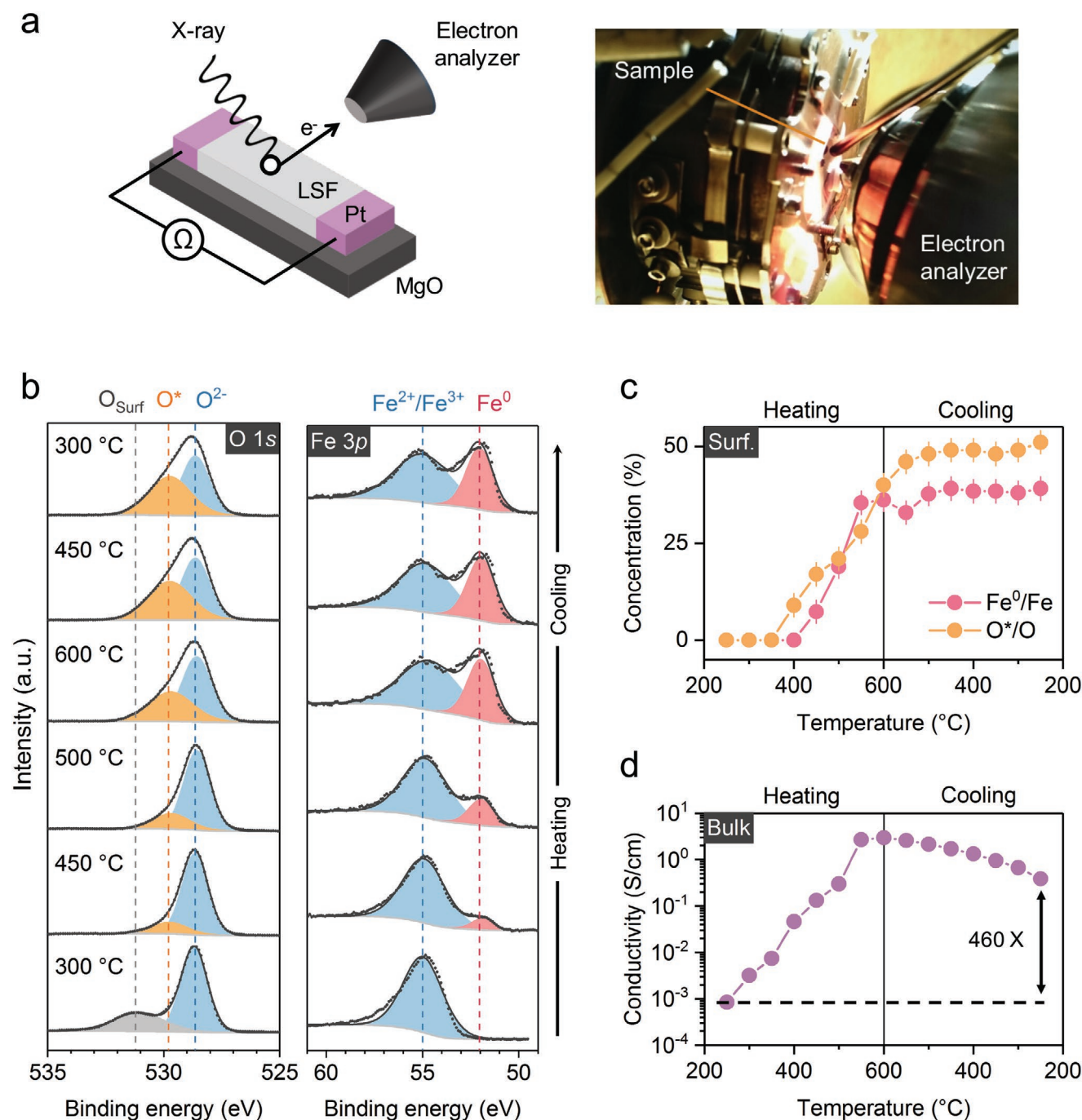


Figure 3. Evolution of surface chemistry and electrical conductivity of LSF upon nanocomposite formation. a) Schematics and photo image of the experimental setup. b) Fe 3p and O 1s NAP-XPS spectra and c) the quantified surface concentrations of Fe^0 and O^* at the LSF surface during heating and cooling in 0.5 Torr H_2 . Origins of each surface species are described in the main text. d) In-plane electrical conductivity of the LSF films during heating and cooling in 0.5 Torr H_2 . Note the Fe^0 exsolution clearly alters both the surface and bulk properties of the LSF.

surface and bulk properties of the LSF film in situ at different stages of Fe^0 exsolution.

The typical O 1s and Fe 3p spectra of the LSF film during Fe^0 exsolution are presented in Figure 3b. We deconvoluted the Fe 3p spectra into two components: one metallic (Fe^0) species at low binding energy and one oxidized iron species (Fe^{2+} and/or Fe^{3+}) at high binding energy.^[67] We are aware

that the peak model is a simplification of the complex Fe peak structure. Nevertheless, utilizing these reduced fitting parameters allowed us to quantify the relative proportions of metallic and oxidized irons at the surface in situ in a facile way. For the O 1s spectra, we identified a total of three oxygen species. The highest binding energy species (denoted as O_{Surf}) is typically assigned to a SrO segregation layer at the

surface of the perovskite.^[68] Since the O_{surf} component only exists before Fe^0 exsolution and irreversibly disappeared after heating in H_2 , we will not discuss it further in this paper. The most intense peak (denoted as O^{2-}) that exists in all the experimental conditions is assigned to the lattice oxygen atoms from the perovskite and/or RP phases.^[69–71] The shoulder feature (denoted as O^*) at ≈ 1.1 eV higher binding energy than the O^{2-} species only appeared after the onset of exsolution and did not vanish even after Ar^+ sputtering under ultra-high vacuum conditions (Note S5, Supporting Information). Therefore, the O^* feature should not originate from surface adsorbates.^[72] Instead, we expect the O^* species to be associated with the non-stoichiometric defect regions that were formed during Fe^0 exsolution. Based on the STEM characterizations presented in the previous section, one such defect region can be the phase boundaries between the metallic iron, RP phase, and the perovskite lattice. While further investigations are required to elucidate the exact chemical nature of the O^* species, its concentration indirectly measures the extent of surface decomposition in LSF during Fe^0 exsolution. As will be shown below, the temporal changes in the intensities of Fe^0 and O^* are consistent with each other, which validates our assignment.

Therefore, we can use the surface concentrations of Fe^0 and O^* to quantitatively determine the extent of exsolution in LSF (Figure 3c). During the heating step, the normalized O 1s intensity gradually decreased (Figure S15, Supporting Information), which indicates oxygen vacancy formation (i.e., lattice reduction).^[37] The Fe^0 species appeared on the surface at 450 °C, which marked the onset of Fe^0 exsolution. Upon further heating in 0.5 Torr H_2 , the surface concentrations of Fe^0 and O^* increased synergistically with temperature, indicating an increasing extent of Fe^0 exsolution in the LSF film. The correlation between the surface concentrations of Fe^0 and O^* further supports our assignment that the O^* species are the side products of Fe^0 exsolution. During the cooling step, the LSF film cannot exchange oxygen with the atmosphere as there is no oxygen source in the chamber.^[73] As a result, the LSF surface maintained a constant stoichiometry during the cooling step, which is exemplified by the invariant Fe^0 and O^* concentration (Figure 3c) and the stable O 1s intensity (Figure S15, Supporting Information). Cooling in H_2 atmosphere thus enables the preservation of the nanocomposite LSF.

Simultaneously with the NAP-XPS measurement, the in-plane DC electrical conductivity of the LSF films was characterized. As shown in Figure 3d, the in-plane electrical conductivity of the film exhibited an asymmetric temperature dependence during respective heating and cooling steps. In particular, the electrical conductivity of the LSF film increased significantly after being heated in H_2 (i.e., after Fe^0 exsolution). As an example, the in-plane conductivity of the LSF film increased by ca. 460 times at 250 °C after Fe^0 exsolution. The appearance of surface Fe^0 and O^* , together with the enhancement in electrical conductivity, clearly demonstrated that Fe^0 exsolution can profoundly modulate the bulk properties of the LSF film. Moreover, the observed increase in surface Fe^0 concentration as well as bulk electrical conductivity (upon nanocomposite formation) are beneficial in improving the electrochemical performance of the materials.^[74–76]

2.3. Tunable Electronic Transport in the Nanocomposite LSF

In this section, we show the enhanced electrical conductivity in the nanocomposite LSF is mainly electronic, highly tunable and arises from the Fe-deficient percolating channels. To do so, we prepared LSF films at three different stages of Fe^0 exsolution: prior to, after medium, and after heavy Fe^0 exsolution. The extent of Fe^0 exsolution in each sample was controlled by monitoring the surface chemistry with NAP-XPS during thermal reduction in 0.5 Torr H_2 . As illustrated in Figure 4a, the LSF sample with the most intense Fe^0 exsolution is featured by the highest surface concentrations of Fe^0 and O^* . The “no exsolution” state in Figure 4 corresponds to the LSF film reduced in 0.5 Torr H_2 at 400 °C, where no Fe^0 can be observed with NAP-XPS (Figure 3c). For each sample, we characterized its electrical conductivity right after sample synthesis in 0.5 Torr H_2 , without air exposure, in the cooling direction. As the electrical conductivity was measured in the cooling direction, the exsolution states in the sample were kinetically trapped. The kinetically trapped exsolution state can be inferred by the stable surface defect chemistry and oxygen non-stoichiometry during the entire conductivity measurement (Figure 3c and Figure S15, Supporting Information). As such, we can directly compare the intrinsic electrical properties of the nanocomposite LSF at different exsolution states. All the conductivity data were obtained after annealing the sample at the highest reduction temperature for ≈ 0.5 h (see Experimental Section). Longer reduction time, however, may result in more exsolved (decomposed) states. Therefore, the conductivity data reported in this study should represent snapshots of certain exsolution states that are defined by both the annealing temperature and time.

The temperature-dependent electrical conductivities (σT) of the nanocomposite LSF films in 0.5 Torr H_2 and in the cooling direction are summarized in Figure 4b. As illustrated, the total electrical conductivity of the LSF film progressively, and substantially increased with the increasing extent of Fe^0 exsolution. As an example, the electrical conductivity of the LSF film increased by more than two orders of magnitude at 400 °C after exsolution. The extent of electrical enhancement was even larger at lower temperatures. In particular, the electrical conductivities for the LSF films at different stages of exsolution all exhibit a temperature-activated, Arrhenius-type behavior. This is interesting as it immediately indicates that the strong enhancement in electrical conductivity does not originate from the metallic phase. In the following paragraphs, we are going to show that the change in the total electrical conductivity mostly likely stems from the formation of the abovementioned percolating Fe-deficient channels in the nanocomposite LSF (see Figure 1).

To resolve the mechanism of enhanced conductivity, we first analyze the evolution in activation energies. As shown in Figure 4b, the reduced perovskite LSF (prior to exsolution) had poor conductivity in H_2 with an activation energy of 1.2 eV. The measured activation energy agrees well with previous studies on the bulk LSF in reducing atmospheres.^[78] The high activation energy suggests that the ionic contribution is significant in the total conductivity, which originates from the minimal concentrations of electrons and holes in the reduced LSF. A detailed defect chemistry and conductivity analysis are

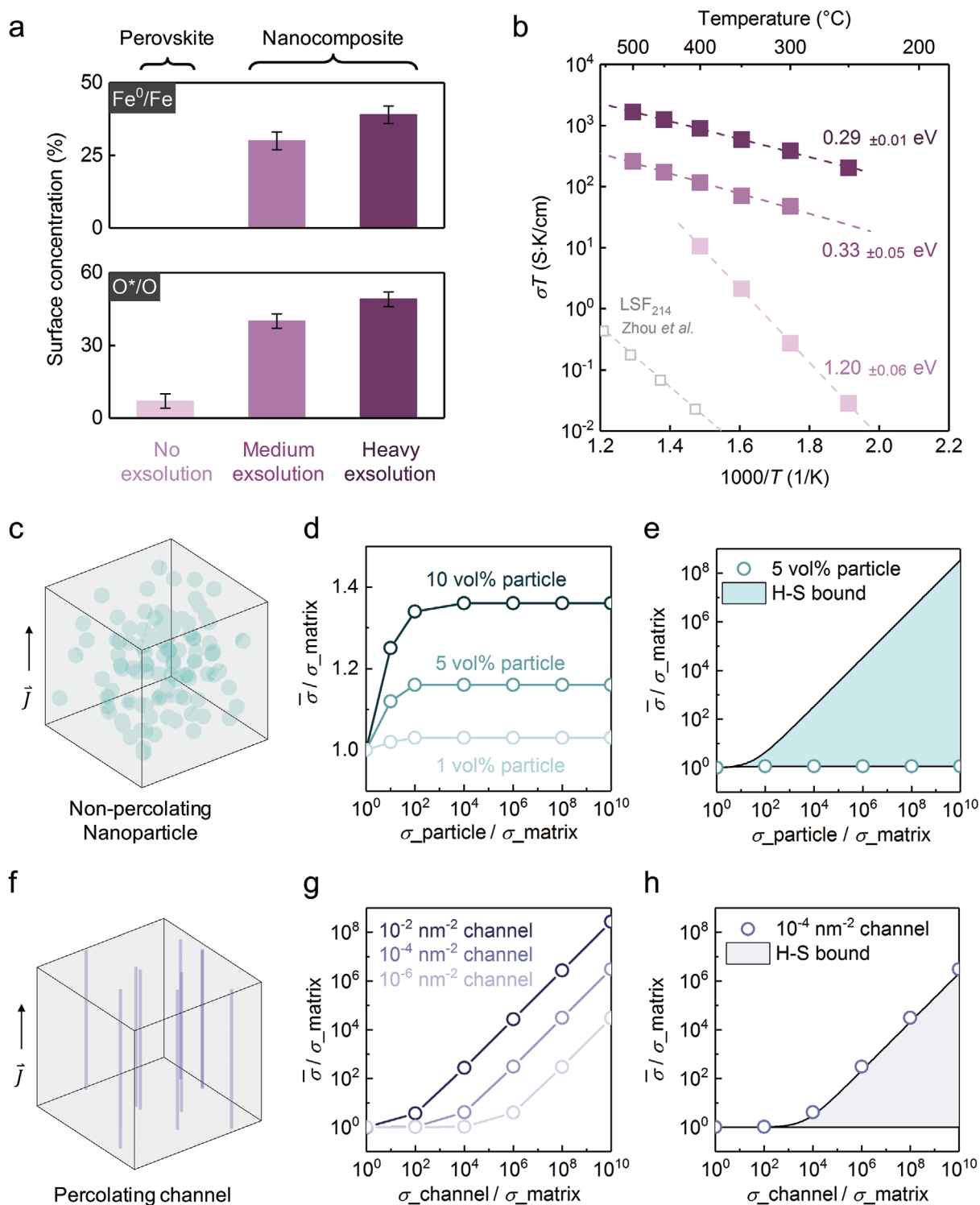


Figure 4. Electrical conductivity of nanocomposites. a) Surface chemistry at three different exsolution stages: before exsolution, medium exsolution, and heavy exsolution (quantified with NAP-XPS). b) In-plane electrical conductivities of the same samples as in (a), where the dashed lines represent the best fit to the Arrhenius relation (see Note S7, Supporting Information). The conductivities were measured in the cooling direction in 0.5 Torr H₂ and the activation energies are presented with 95% confidence interval. The color codes in (b) are the same as in (a). The electrical conductivities of the RP phase La_{1.2}Sr_{0.8}FeO₄ (denoted as “LSF₂₁₄”) in 5% H₂/Ar atmosphere^[77] are also shown for comparison. c–h) Finite element analysis (FEA) of the contributions from the non-percolating nanoparticles and percolation channels to the electrical conductivity enhancement. c, f) FEA models. d, g) Electrical conductivity of the nanocomposite as a function of (d) nanoparticle density, and (g) channel density. e, h) Comparison of the finite element calculation to the Hashin–Shtrikman (H–S) bounds. Note the percolating channels are more effective in increasing the total electrical conductivity than the non-percolating nanoparticles.

presented in the Note S6, Supporting Information. After Fe⁰ exsolution, the activation energy decreased from 1.2 to ≈0.3 eV for both the medium- and heavily-exsolved LSF films. The low activation energies indicate that the electronic conduction dominates the nanocomposite LSF, which was further supported by the impedance characterization (Note S7, Supporting Information). Therefore, based on the activation energy and impedance analysis, we confirmed that the electronic contributions dominate the total conductivity in the nanocomposite LSF. In other words, in the experimental conditions of this work, Fe exsolution turns LSF from a dominantly ionic conductor and electronic insulator, to a dominantly electronic conductor. When varying the extent of exsolution in a nanocomposite LSF, above the limit where a new conduction mechanism dominates, one tailors the concentration of charge carriers. That means the conduction mechanism remains the same for the medium and heavily exsolved LSF films, evident from their identical activation energies.

We then assess the different components of the exsolved LSF and demonstrate that the enhanced electronic conductivities should originate from the percolating channels. First of all, we show that the conductivity enhancement does not originate from the LSF₁₁₃ perovskite phase. As illustrated above (Figure 4b and Note S7, Supporting Information) and also in other studies,^[35,36] the perovskite matrix became off-stoichiometric during the exsolution process. Such off-stoichiometry in the LSF matrix can strongly decrease its electronic conductivity. This is because the electronic conduction in the LSF lattice occurs along Fe–O–Fe chains,^[79,80] and a disruption of these chains by the introduction of oxygen and Fe vacancies would impede the hopping of the electronic charge carriers.^[81] In support of this model, both oxygen and B-site vacancy formation were found to lower the electrical conductivity in LSF^[81] and other perovskite systems.^[40,82]

Second, we show that the formation of RP-type LSF₂₁₄ during exsolution does not explain the observed conductivity enhancement. As shown in Figure 2, we observed RP phase formation in the bulk lattice during Fe⁰ exsolution. To assess the effect of the RP phase formation on the total conductivity change, we plotted the conductivity of the La_{1.2}Sr_{0.8}FeO₄ in Figure 4b (data from ref. [77] measured in 5% H₂/Ar gas atmosphere). As illustrated, La_{1.2}Sr_{0.8}FeO₄ exhibited a much lower electrical conductivity than the perovskite phase LSF in H₂ atmosphere. Consequently, we expect the formation of only RP phase as a by-product to Fe⁰ exsolution would rather decrease the total electrical conductivity of the film instead of increasing it.

Third, we show that the formation of the exsolved Fe⁰ nanoparticles cannot explain the conductivity enhancement, either, because they are not percolated as seen in the STEM images in Figure 1. For this, we conducted finite element analysis (FEA) to calculate how the total conductivity is affected by the conductivity and density of the exsolved nanoparticles. As shown in Figure 4c, the nanoparticles were modeled as homogeneously dispersed spheres of 5 nm radius (see Experimental Section for the detailed modeling description). According to the magnetic measurement, the total volume fraction of the Fe⁰ nanoparticles in the exsolved LSF film was around 6% (Note S8, Supporting Information). Therefore, we varied the volume concentrations of the spheres between 0 and 10% in the FEA

modeling and the results are displayed in Figure 4d. For better visualization, we normalized the particle conductivity (σ_{particle}) and the spatially averaged total conductivity ($\bar{\sigma}$) to that of the LSF matrix (σ_{matrix}). As shown in Figure 4d, the introduction of non-percolating nanoparticles to the matrix has minimal impact on the total conductivity. By increasing the particle conductivities ($\sigma_{\text{particle}}/\sigma_{\text{matrix}}$) from 10⁰ to 10¹⁰, the total conductivity of the nanocomposite ($\bar{\sigma}/\sigma_{\text{matrix}}$) can only increase up to 40%. Therefore, the non-percolating nanoparticles cannot explain the more than 100 times higher electrical conductivity observed in Figure 3d.

Finally, we show that the percolating channels can substantially modulate the total electrical conductivity of the exsolved LSF film. As shown in Figure 1d, Fe⁰ exsolution forms both in-plane and cross-plane percolating channels in the LSF matrix. Since the channels that are perpendicular to the electrical current have negligible impact on the total electrical conductivity (Note S9, Supporting Information), we focus on the channels that percolate in the same direction as the electrical currents (i.e., the in-plane direction). While the channels can be 2D shapes traversing the matrix, we modeled the channels as cylinders oriented parallel to the electrical current for computational efficiency (Figure 4f). Based on the STEM characterizations (Figure 1e), we set the cylinder radius to be 1 nm and varied the cylinder densities (i.e., the total channel length per unit volume) between 10⁻⁶ to 10⁻² cm⁻² in the model. As shown in Figure 4g, we find the total conductivity ($\bar{\sigma}/\sigma_{\text{matrix}}$) increased significantly with the channel conductivity ($\sigma_{\text{channel}}/\sigma_{\text{matrix}}$), evident from the logarithmic scale in the plot. To further elucidate the role of percolating channels in modulating the total conductivity, we compared our modeling to the theoretical Hashin–Shtrikman (H–S) bounds.^[83] As indicated by the shaded regions in Figure 4e,h, the H–S bounds provide theoretical bounds for the macroscopic electrical conductivity of isotropic two-phase media of arbitrary phase geometry. As illustrated, the non-percolating nanoparticles and percolating channels essentially represent the lower and upper H–S bounds, respectively.

Based on these results, we expect the electronic conductivity enhancement in the nanocomposite LSF can only originate from the formation of percolating channels. Several factors could contribute to the observed enhanced electronic conductivities. First, as revealed by the EDX mapping (Figure 1e) and XPS analysis (Figure 3c and Note S10, Supporting Information), the percolating channels can be highly off-stoichiometric and contain high concentrations of lattice defects. Due to charge neutrality, the off-stoichiometry and lattice defects in the percolating channels may lead to locally enriched electronic charge carriers, which can result in an apparent higher electronic conductivity. Second, the observed electronic conductivity enhancement may also originate from interface effects. As discussed in Figures 1 and 2, many of the percolating channels are located near the phase boundaries. Such heterostructures may also lead to emergent transport properties.^[6–9] For example, Chang et al. observed a confined polaronic transport near the LaFeO₃/SrFeO₃ interface, which results in a significantly enhanced electronic conductivity as well as a reduction in the activation energy.^[84] Previous studies have also demonstrated that the space-charge layer near the extended defects can significantly modulate the total electronic conductivities of the oxides.^[39,85,86]

While further studies are needed to elucidate the detailed conduction mechanisms, our results unambiguously demonstrate that Fe⁰ exsolution can be used as an effective tuning parameter to tailor the electronic conductivities of the nanocomposite LSF.

2.4. Tuning Nanocomposite Magnetism via Redox Switching

As seen in recent exciting studies, oxygen non-stoichiometry in oxides can be utilized to control the materials' magnetic properties.^[87–89] Motivated by this idea, we demonstrate in this section that one can further modulate the magnetism of the nanocomposite LSF via reversible redox switching of the precipitated Fe nanoparticles. To examine the redox behavior of the nanocomposite LSF, we cycled the exsolved LSF film between 0.2 Torr O₂ and 0.5 Torr H₂ at 400 °C (for experimental details, see Note S10, Supporting Information). The temperature is chosen to be below the exsolution onset (450 °C, see Figure 3) so that no additional exsolution would occur from the host oxide.

The in situ NAP-XPS analysis of the nanocomposite LSF during the redox cycles is summarized in Figure 5a–c. First, after each oxidation treatment, the Fe⁰ species disappeared and the O* concentration decreased to ≈10%. These findings indicate that the oxidative treatment not only oxidized the surface Fe⁰ nanoparticles, but also partially recovered the surface defects that had been formed in exsolution. Second, after the successive reduction treatment, the Fe⁰ species appeared again on the surface, together with an increase in the O* concentration. Since the reduction temperature is below the exsolution onset, no further Fe⁰ exsolution should occur. Therefore, the resurgence of Fe⁰ and O* indicates that the surface Fe⁰ nanoparticles did not reintegrate into the host oxide upon re-oxidation, but were oxidized to iron oxides. Ex situ AFM measurements also confirmed that the nanoparticles did not dissolve upon re-oxidation (Note S10, Supporting Information). This is reasonable because the exsolved nanoparticles would only dissolve at very high temperatures.^[19,26–28] On the other hand, mild oxidation would only oxidize the Fe⁰ nanoparticles into iron oxides.^[30] Then, the successive reduction process reduced these iron oxides back to Fe⁰ and (partially) regenerated the surface defects (i.e., the O* species). As the reduction temperature (400 °C) is lower than that of the exsolution condition (600 °C, see Figure 3), the surface concentrations of Fe⁰ and O* after the re-reduction step were smaller than that of the as-exsolved LSF surface (cycle 0).

Therefore, Figure 5a–c unambiguously demonstrates that both the surface exsolved iron nanoparticles (featured by the surface Fe⁰ species) and the surface oxide lattice (featured by surface O*) can reversibly exchange oxygen with the gas atmosphere even at temperatures below the exsolution onset. As stated in the Introduction section, the unique redox capability to cycle exsolved Fe nanoparticles between the metallic and oxide states is crucial in both catalytic activity switching^[30] as well as catalyst regeneration.^[19,31] The highly reversible surface chemistry during the redox cycling also highlights the redox stability of the nanocomposite LSF film.

Having demonstrated the reversible surface redox capability, we then turn to the bulk redox properties of the nanocomposite LSF. To probe the phase evolution of the embedded nanoparticles, we employed magnetic measurements due to

their exceptional sensitivity to the ferromagnetic exsolved nanoparticles.^[90,91] As metallic iron has much higher magnetization than the iron oxides, oxidation of the embedded Fe⁰ nanoparticles should result in a decreased saturation magnetization.^[92,93] Therefore, the saturation magnetization of the LSF nanocomposite can be used to estimate the oxidation state of the exsolved nanoparticles. We employed vibrating-sample magnetometry (VSM) to probe the magnetic property of the nanocomposite LSF at different stages of the redox cycling: as-exsolved, mildly oxidized, and heavily oxidized. The surface chemistry of each sample before taking out of the XPS chamber is shown in Figure 5d.

Figure 5e summarizes the room-temperature in-plane magnetic hysteresis loops of these three samples, along with that of the as-prepared state. As illustrated, the as-prepared LSF film shows negligible magnetic hysteresis, which is consistent with the reported weak ferromagnetism in La_{0.6}Sr_{0.4}FeO₃ (Ref. [94]). After Fe⁰ exsolution, however, magnetic hysteresis (*M*–*H*) loops are clearly present at room temperature with a saturation magnetization (*M*_S) of about 110 emu cm^{−3} (normalized by the entire volume of LSF film). Since both the reduced perovskite LSF matrix (Note S11, Supporting Information) and the RP phase LSF₂₁₄ (ref. [95]) have negligible magnetic properties, the enhanced magnetism is due to the formation of ferromagnetic exsolved nanoparticles. Since the embedded Fe⁰ nanoparticles can maintain their metallic state even upon air exposure at room temperature (Figure 2), we expect the magnetism of the as-exsolved LSF to be mainly determined by the Fe⁰ nanoparticles embedded within the LSF film. In accordance with the isotropic geometry and uniform spatial distribution of the exsolved Fe⁰ nanoparticles (Figure 1), the nanocomposite LSF exhibited similar in-plane and out-of-plane magnetic properties (Note S11, Supporting Information). If the Fe nanoparticles have the bulk magnetization of iron, the net magnetization of the film implies 6% by volume of nanoparticles. The estimated volume fraction agrees well with the TEM observation, where the particle area fraction is ≈8% (Note S8, Supporting Information).

The successive oxidation treatment progressively reduced the saturation magnetization to ≈25 emu cm^{−3}. As the oxidation temperature is too low for the exsolved nanoparticles to reintegrate into the lattice (Note S10, Supporting Information), the decrease in the total saturation magnetization originates from the oxidation of the embedded Fe⁰ nanoparticles into iron oxides. A likely scenario would be that the re-oxidation process occurred via the growth of oxide shells at the expense of Fe⁰ cores, forming core-shell structures during the evolution of oxidation. A similar phenomenon has also been observed in the oxidation of iron nanoparticles.^[93] In accord with this hypothesis, the coercivity of the nanocomposite LSF also decreased upon re-oxidation (inset figure in Figure 5e). Since the embedded Fe⁰ particles in the nanocomposite LSF adopt single-domain structures (Note S8, Supporting Information), a decrease in coercivity is consistent with a reduction in size of the Fe⁰ core and in the thermal stability of the magnetization upon oxidation.^[96] The continuous modulation of the saturation magnetization and coercivity of the nanocomposite LSF thus reflects the reversible oxidation of the embedded Fe⁰ nanoparticles. Moreover, our observations demonstrate one can realize a multiple-state control of the nanocomposite LSF via oxygen

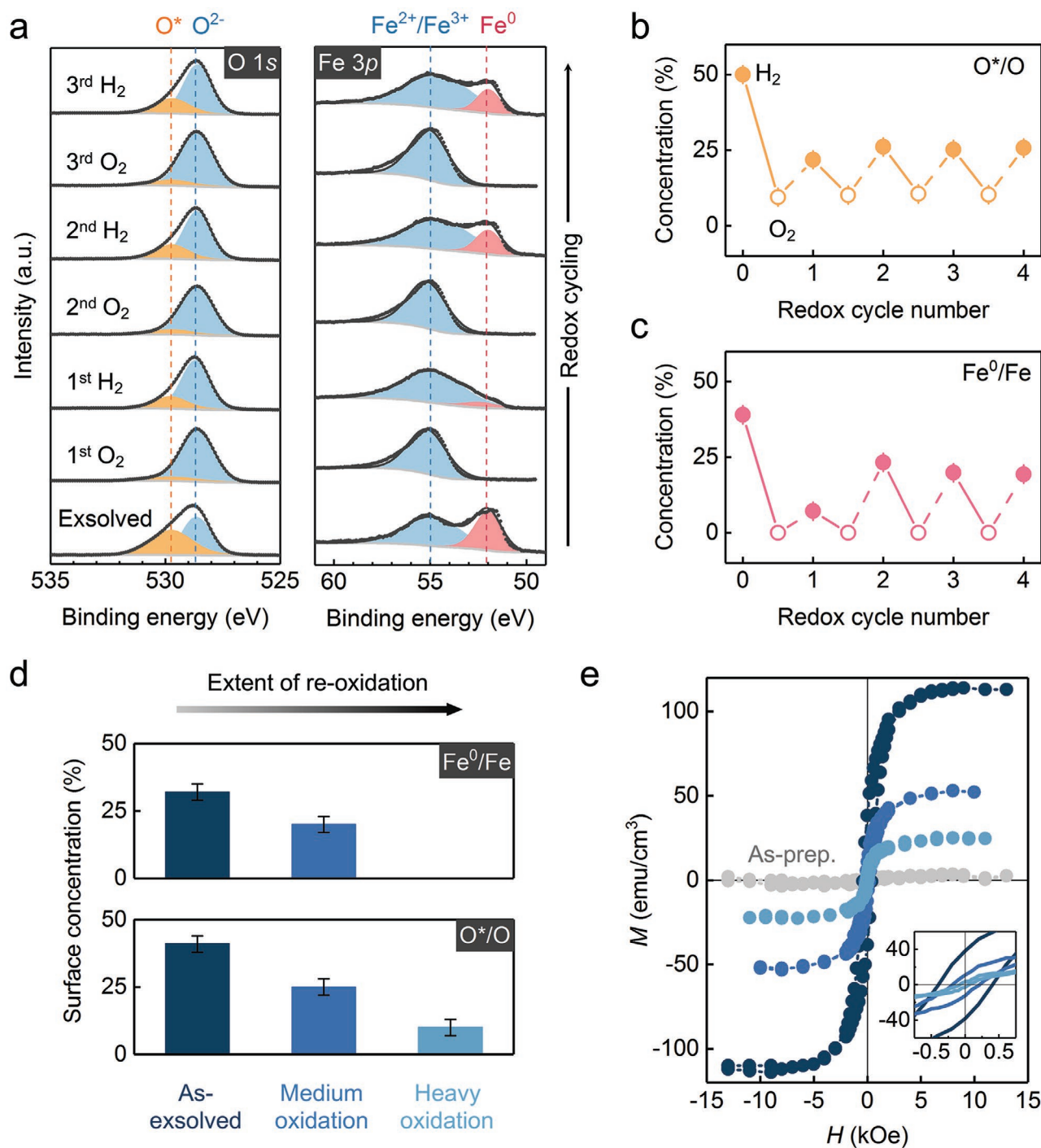


Figure 5. Redox properties of the nanocomposite LSF. a) NAP-XPS Fe 3p and O 1s spectra, surface concentrations of b) O*, and c) Fe⁰ of the exsolved LSF film during redox cycling between 0.2 Torr O₂ (empty symbols) and 0.5 Torr H₂ (solid symbols) at 400 °C. The solid and dashed lines in plot (b) and (c) indicate the oxidation and reduction step, respectively. Here, cycle 0 represents the as-exsolved state. d) In situ surface chemistry quantified with NAP-XPS and e) ex situ room temperature magnetization versus field (M–H) loops of the LSF films at different stages of the redox cycling: as-exsolved, medium oxidized, and heavily oxidized. The color codes in (e) are the same as in (d). Meanwhile, the as-prepared LSF (without exsolution) is also shown in (e) for comparison. M is normalized to the total volume of the film. The inset figure in (e) highlights the decrease in coercivity upon re-oxidation.

non-stoichiometry. The tuning range of the magnetic moment in the nanocomposite LSF (from zero to ≈110 emu cm⁻³) is comparable to other state-of-art perovskite systems.^[97] While we demonstrate here the modulation of magnetism modulation

at elevated temperatures and slow rate, the switching could potentially be done at a much faster rate and at room temperature if we use electrochemistry to trigger the redox switching.^[30,97,98] Therefore, redox switching can be an effective

“tuning knob” to dynamically manipulate the microstructure, phase composition, and magnetic properties of the exsolved nanocomposite.

3. Conclusion

In summary, this study demonstrates a novel utility of exsolution in preparing nanostructured, multi-phase metal oxides with tunable properties. First, we showed that Fe⁰ exsolution can induce a drastic chemical and structural reorganization both at the surface and in the bulk of LSF, transforming the single-phase perovskite into a multi-phase nanocomposite that consists of Fe⁰ nanoparticles, crystalline RP domains, and percolated Fe-deficient nm-scale channels. Second, by comparing nanocomposite LSF at different stages of Fe⁰ exsolution, we demonstrated that the extent of Fe⁰ exsolution can be used as an effective tool to tailor the chemical, electrical, and magnetic properties of the nanocomposite LSF. We found that, in addition to the exsolved nanoparticles, the exsolution-induced lattice defects can profoundly impact the properties of the material. In particular, we observed an increase in the electronic conductivity by more than two orders of magnitude, turning LSF from a dominantly ionic conductor to a dominantly electronic conductor. With the aid of numerical analysis, we demonstrated that such a large change in conductivity can only arise from the Fe-deficient percolating channels formed during exsolution in this structure. Moreover, as both the surface and the embedded exsolved Fe nanoparticles are highly redox active, the magnetic properties of the nanocomposite LSF can be modulated via redox control. At moderate temperatures even below the exsolution onset, we achieved a continuous control of the magnetic properties of the nanocomposite LSF between 0 and 110 emu cm⁻³. Besides the temperature and gas atmospheres that are used in this work, other external stimuli such as electrochemical overpotential^[30] and photo-illumination^[99] could also be employed to tailor exsolution, and hence the geometry and functionalities of the resulting nanocomposite. Moreover, while this paper focused on the thin-film system, it is conceivable that one can also synthesize bulk versions of nanocomposite materials via exsolution. The findings of this work thus highlight the potential of bulk exsolution in synthesizing tunable multifunctional nanocomposites, which can benefit a broad range of applications including SOC, nanophotonics, thermoelectric devices, multiferroics, and memory/logic technologies.

4. Experimental Section

Sample Preparation: The thin-film La_{0.6}Sr_{0.4}FeO₃ (LSF) was deposited using PLD with a KrF ($\lambda = 248$ nm) excimer laser. Insulating 10 mm × 5 mm × 0.5 mm MgO (001) single crystal substrates (MTI Corporation, 1-side polished) were employed in this work to minimize substrate leakage current during the conductivity measurement. For film deposition, the backside substrate temperature was kept at 850 °C (which approximately corresponds to 650 °C film temperature) in an oxygen pressure of 20 mTorr. By applying 30 000 laser pulses (5 Hz, 1.5 mJ cm⁻²) to the LSF target, a LSF thin film of ca. 120 nm thickness was grown on the substrate. After deposition, 5 nm Ti followed by 100 nm Pt were deposited as electrical contacts onto the film surface using magnetron sputtering.

Thin-Film Characterization: AFM images were collected on a Cypher S AFM Microscope with tapping mode, using a Bruker TESP-V2 AFM probe. The AFM characterization was done on the center of the sample to avoid edge effects. XRD measurements were conducted with Rigaku SmartLab X-ray diffractometer using Cu K α 1 radiation.

Near-Ambient Pressure XPS (NAP-XPS) Measurement: The in situ NAP-XPS measurements were carried out at the IOS (23-ID-2) beamline of the National Synchrotron Light Source II (NSLS-II) at Brookhaven National Lab. The sample was placed on a ceramic button heater, with a K-type thermocouples mounted directly onto the surface for temperature measurements. The LSF films were preconditioned at 400 °C in 0.2 Torr O₂ at the beginning of each measurement to remove adventitious carbon. At each temperature, the data was collected after waiting for 15 min. As the NAP-XPS measurements took about around 25 min, the time spent at each temperature was around 40 min. The electrical measurements were conducted with a Keithley 2461 Sourcemeter, available at the beamline. During the NAP-XPS measurement, the in-plane electrical measurements were carried out in a 2-probe geometry on the LSF film. Representative current-voltage characteristics of the LSF films are shown in Note S7, Supporting Information. All the NAP-XPS spectra were quantified with CasaXPS software. The XPS peaks were fitted with a 30% Lorentz/Gaussian line shape over a Shirley background.

X-Ray Absorption Spectroscopy (XAS): Ex situ XAS were collected by partial fluorescence yield (PFY) modes at the IOS beamline of NSLS-II. PFY spectra were collected at room temperature in an ultrahigh-vacuum chamber (base pressure, $\approx 10^{-9}$ torr), using a Vortex silicon drift detector. In situ XAS were collected using the partial electron yield (PEY) method at Beamline 9.3.2 of the Advanced Light Source (ALS), Lawrence Berkeley National Laboratory.

Scanning Transmission Electron Microscopy (STEM) – Energy Dispersive X-Ray Spectroscopy (EDX) Characterization: LSF films were characterized using a state-of-the-art aberration-corrected JEOL Grand ARM300CF STEM operated at 300 keV. This instrument was equipped with dual silicon drift detectors for EDX with a total detector area of 200 mm². Gatan Microscopy Suite (GMS version 3) software was used for STEM-EDS elemental mapping using these EDS peaks: O K α (0.52 keV), Fe K α and K β (6.40 and 7.06 keV respectively), La L α and L β (4.65 and 5.04 keV respectively), and Sr K α and K β (14.16 and 15.84 keV respectively). FFT analysis on the STEM images, using the Gatan Microscopy Suite and ImageJ, was also performed to identify the phases in the LSF exsolved film.

Finite Element Analysis (FEA): The Poisson–Boltzmann equation was solved to obtain the nanocomposite electrical conductivity. The LSF matrix was modeled as a homogeneous 100 × 100 × 100 nm³ cube, while the nanoparticles and the percolating channels were idealized as homogeneous spheres (5 nm in radius) and cylinders (radius 1 nm and height 100 nm), respectively. The geometry of these two objects was set based on their average dimensions, which were quantified by the cross-sectional STEM imaging. In this model, the nanoparticles and percolating channels were randomly generated in the matrix without intersection. All the materials properties in the FEA modeling were homogeneous and isotropic. The FEA analysis was coded in MATLAB.

Magnetic Properties Characterization: The magnetic hysteresis loops were measured using a Digital Measurement System 7035B VSM at room temperature. During the VSM measurement, the magnetic field was applied parallel to the sample surface (i.e., in-plane direction). The data processing procedure is presented in Note S11, Supporting Information.

Supporting Information

Supporting Information is available from the Wiley Online Library or from the author.

Acknowledgements

The authors would like to thank the Exelon Corporation and the MIT Energy Initiative Seed Fund Program for supporting the work presented in this paper. This research used the synchrotron radiation facilities at the National Synchrotron Light Source II (IOS/23-ID-2 beamline), a U.S. Department of Energy (DOE) Office of Science User Facility operated for the DOE Office of Science by Brookhaven National Laboratory under Contract No. DE-SC0012704; and the Advanced Light Source which was supported by the DOE Office of Basic Energy Sciences under Contract No. DE-AC02-05CH11231. For STEM-EDS characterization work, the authors acknowledge the use of facilities and instrumentation at the UC Irvine Materials Research Institute (IMRI), which is supported in part by the National Science Foundation through the UC Irvine Materials Research Science and Engineering Center (DMR-2011967). J.W. thanks Dimitrios Fraggadakis (MIT) for the helpful discussions on the Hashin–Shtrikman bounds. J.W. thanks Andreas Nenning (TU Wien) for the assistance on the Van der Pauw measurements. W.J.B. acknowledges UCI new faculty start-up funding. K.S. acknowledges support from US Department of Education Graduate Assistance in Areas of National Need (GAANN) Fellowship. C.R. and S.N. acknowledge support from NSF DMR 1419807.

Conflict of Interest

The authors declare no conflict of interest.

Authors Contribution

J.W. and B.Y. conceived the experiment design. J.W. prepared the samples and analyzed the data. J.W., I.W., A.H., and E.J.C. carried out the synchrotron experiments. K.S. and W.J.B. conducted the STEM imaging. S.N. conducted the VSM measurement. J.W. conducted the finite element analysis. J.W. wrote the manuscript and all authors contributed to its revision. B.Y. supervised the project.

Data Availability Statement

The data that support the findings of this study are available from the corresponding author upon reasonable request.

Keywords

exsolution, multi-functionality, nanocomposites, self-assembly, thin films

Received: August 11, 2021

Revised: October 23, 2021

Published online:

- [1] M. Acosta, F. Baiutti, A. Tarancón, J. L. MacManus-Driscoll, *Adv. Mater. Interfaces* **2019**, *6*, 1900462.
- [2] A. Chen, Q. Su, H. Han, E. Enriquez, Q. Jia, *Adv. Mater.* **2019**, *31*, 1803241.
- [3] C. Benel, T. Reisinger, R. Kruk, H. Hahn, *Adv. Mater.* **2019**, *31*, 1806634.
- [4] F. Baiutti, F. Chiabrera, M. Acosta, D. Diercks, D. Parfitt, J. Santiso, X. Wang, A. Cavallaro, A. Morata, H. Wang, A. Chronos, J. MacManus-Driscoll, A. Tarancón, *Nat. Commun.* **2021**, *12*, 2660.
- [5] Y. Chen, Z. Cai, Y. Kuru, W. Ma, H. L. Tuller, B. Yildiz, *Adv. Energy Mater.* **2013**, *3*, 1221.
- [6] X. Guo, J. Maier, *Adv. Mater.* **2009**, *21*, 2619.

- [7] H. Yao, Y.-P. Hsieh, J. Kong, M. Hofmann, *Nat. Mater.* **2020**, *19*, 745.
- [8] A. Ohtomo, H. Y. Hwang, *Nature* **2004**, *427*, 423.
- [9] N. Sata, K. Eberman, K. Eberl, J. Maier, *Nature* **2000**, *408*, 946.
- [10] R. Ramesh, N. A. Spaldin, *Nat. Mater.* **2007**, *6*, 21.
- [11] W. Ma, J. J. Kim, N. Tsvetkov, T. Daio, Y. Kuru, Z. Cai, Y. Chen, K. Sasaki, H. L. Tuller, B. Yildiz, *J. Mater. Chem. A* **2015**, *3*, 207.
- [12] C. Su, W. Wang, M. Liu, M. O. Tadé, Z. Shao, *Adv. Energy Mater.* **2015**, *5*, 1500188.
- [13] J. Wang, L. Li, H. Huyen, X. Pan, S. S. Nonnenmann, *Adv. Funct. Mater.* **2019**, *29*, 1808430.
- [14] J. H. Yoon, J. H. Han, J. S. Jung, W. Jeon, G. H. Kim, S. J. Song, J. Y. Seok, K. J. Yoon, M. H. Lee, C. S. Hwang, *Adv. Mater.* **2013**, *25*, 1987.
- [15] J. Spring, E. Sediva, Z. D. Hood, J. C. Gonzalez-Rosillo, W. O'leary, K. J. Kim, A. J. Carrillo, J. L. M. Rupp, *Small* **2020**, *16*, 2003224.
- [16] H. C. Hendrikse, A. Weijden, M. Ronda-Lloret, T. Yang, R. Bliem, N. R. Shiju, M. Hecke, L. Li, W. L. Noorduin, *Adv. Mater.* **2020**, *32*, 2003999.
- [17] G. Tsekouras, D. Neagu, J. T. S. Irvine, *Energy Environ. Sci.* **2013**, *6*, 256.
- [18] D. Neagu, G. Tsekouras, D. N. Miller, H. Ménard, J. T. S. Irvine, *Nat. Chem.* **2013**, *5*, 916.
- [19] Y. Nishihata, J. Mizuki, T. Akao, H. Tanaka, M. Uenishi, M. Kimura, T. Okamoto, N. Hamada, *Nature* **2002**, *418*, 164.
- [20] K. Kousi, C. Tang, I. S. Metcalfe, D. Neagu, *Small* **2021**, *17*, 2006479.
- [21] P. Munnik, P. E. de Jongh, K. P. Jong, *Chem. Rev.* **2015**, *115*, 6687.
- [22] H. Han, J. Park, S. Y. Nam, K. J. Kim, G. M. Choi, S. S. P. Parkin, H. M. Jang, J. T. S. Irvine, *Nat. Commun.* **2019**, *10*, 1471.
- [23] K. Kousi, D. Neagu, L. Bekris, E. Cali, G. Kerherve, E. I. Papaioannou, D. J. Payne, I. S. Metcalfe, *J. Mater. Chem. A* **2020**, *8*, 12406.
- [24] K. Kousi, D. Neagu, L. Bekris, E. I. Papaioannou, I. S. Metcalfe, *Angew. Chem., Int. Ed.* **2020**, *59*, 2510.
- [25] M. L. Weber, M. Wilhelm, L. Jin, U. Breuer, R. Dittmann, R. Waser, O. Guillon, C. Lenser, F. Gunkel, *ACS Nano* **2021**, *15*, 4546.
- [26] K.-Y. Lai, A. Manthiram, *Chem. Mater.* **2018**, *30*, 2838.
- [27] S. Dai, S. Zhang, M. B. Katz, G. W. Graham, X. I. Pan, *ACS Catal.* **2017**, *7*, 1579.
- [28] M. B. Katz, S. Zhang, Y. Duan, H. Wang, M. Fang, K. Zhang, B. Li, G. W. Graham, X. Pan, *J. Catal.* **2012**, *293*, 145.
- [29] D. Neagu, T.-S. Oh, D. N. Miller, H. Ménard, S. M. Bukhari, S. R. Gamble, R. J. Gorte, J. M. Vohs, J. T. S. Irvine, *Nat. Commun.* **2015**, *6*, 8120.
- [30] A. K. Opitz, A. Nenning, V. Vonk, S. Volkov, F. Bertram, H. Summerer, S. Schwarz, A. Steiger-Thirsfeld, J. Bernardi, A. Stierle, J. Fleig, *Nat. Commun.* **2020**, *11*, 4801.
- [31] H. Lv, L. Lin, X. Zhang, Y. Song, H. Matsumoto, C. Zeng, N. Ta, W. Liu, D. Gao, G. Wang, X. Bao, *Adv. Mater.* **2020**, *32*, 1906193.
- [32] G. Dimitrakopoulos, A. F. Ghoniem, B. Yildiz, *Sustainable Energy Fuels* **2019**, *3*, 2347.
- [33] J. T. S. Irvine, D. Neagu, M. C. Verbraeken, C. Chatzichristodoulou, C. Graves, M. B. Mogensen, *Nat. Energy* **2016**, *1*, 15014.
- [34] J. Li, M.-X. Guan, P.-F. Nan, J. Wang, B.-H. Ge, K.-M. Qiao, H.-R. Zhang, W.-H. Liang, J.-Z. Hao, H. B. Zhou, F.-R. Shen, F.-X. Liang, C. Zhang, M. Liu, S. Meng, T. Zhu, F.-X. Hu, T. Wu, J.-D. Guo, J.-R. Sun, B.-G. Shen, *Nano Energy* **2020**, *78*, 105215.
- [35] O. Kwon, S. Sengodan, K. Kim, G. Kim, H. Y. Jeong, J. Shin, Y.-W. Ju, J. W. Han, G. Kim, *Nat. Commun.* **2017**, *8*, 15967.
- [36] A. S. Raman, A. Vojvodic, *Chem. Mater.* **2020**, *32*, 9642.
- [37] J. Wang, J. Yang, A. K. Opitz, W. Bowman, R. Bliem, G. Dimitrakopoulos, A. Nenning, I. Waluyo, A. Hunt, J.-J. Gallet, B. Yildiz, *Chem. Mater.* **2021**, *33*, 5021.
- [38] D. Chen, C. Chen, Z. M. Baiyee, Z. Shao, F. Ciucci, *Chem. Rev.* **2015**, *115*, 9869.
- [39] P. Lupetin, G. Gregori, J. Maier, *Angew. Chem., Int. Ed.* **2010**, *49*, 10123.

- [40] C. R. Smith, A. C. Lang, V. Shutthanandan, M. L. Taheri, S. J. May, *J. Vac. Sci. Technol.*, A **2015**, 33, 041510.
- [41] W. Dieterich, O. Dürr, P. Pendzig, A. Bunde, A. Nitzan, *Phys. A* **1999**, 266, 229.
- [42] H. S. Lee, S. D. Findlay, T. Mizoguchi, Y. Ikuhara, *Ultramicroscopy* **2011**, 111, 1531.
- [43] N. Twu, X. Li, A. Urban, M. Balasubramanian, J. Lee, L. Liu, G. Ceder, *Nano Lett.* **2015**, 15, 596.
- [44] F. M. Draber, C. Ader, J. P. Arnold, S. Eisele, S. Grieshammer, S. Yamaguchi, M. Martin, *Nat. Mater.* **2020**, 19, 338.
- [45] Y. Kim, J. Zhu, B. Yeom, M. Di Prima, X. Su, J.-G. Kim, S. J. Yoo, C. Uher, N. A. Kotov, *Nature* **2013**, 500, 59.
- [46] H. E. Swanson, *Standard X-ray Diffraction Powder Patterns*, Vol. 7, US Department of Commerce, National Bureau of Standards, Gaithersburg, Maryland, USA **1953**.
- [47] L. W. Finger, R. M. Hazen, A. M. Hofmeister, *Phys. Chem. Miner.* **1986**, 13, 215.
- [48] D. Schulz, G. McCarthy, *ICDD Grant-in-Aid*, North Dakota State University, Fargo, ND, USA **1987**.
- [49] G. Li, J. Lan, G. Li, *RSC Adv.* **2015**, 5, 1705.
- [50] W. Jian, R. Jia, J. Wang, H.-X. Zhang, F.-Q. Bai, *Inorg. Chem. Front.* **2019**, 6, 2810.
- [51] D. Neagu, E. I. Papaioannou, W. K. W. Ramli, D. N. Miller, B. J. Murdoch, H. Ménard, A. Umar, A. J. Barlow, P. J. Cumpson, J. T. S. Irvine, I. S. Metcalfe, *Nat. Commun.* **2017**, 8, 1855.
- [52] S. E. Dann, D. B. Currie, M. T. Weller, M. F. Thomas, A. D. Al-Rawwas, *J. Solid State Chem.* **1994**, 109, 134.
- [53] N. Qureshi, H. Ulbrich, Y. Sidis, A. Cousson, M. Braden, *Phys. Rev. B* **2013**, 87, 054433.
- [54] L. Mohaddes-Ardabili, H. Zheng, S. B. Ogale, B. Hannoyer, W. Tian, J. Wang, S. E. Lofland, S. R. Shinde, T. Zhao, Y. Jia, L. Salamanca-Riba, D. G. Schlom, M. Wuttig, R. Ramesh, *Nat. Mater.* **2004**, 3, 533.
- [55] J. Li, Y. Yu, Y.-M. Yin, N. Zhou, Z.-F. Ma, *Electrochim. Acta* **2017**, 235, 317.
- [56] T. Götsch, N. Köpfler, L. Schlicker, E. A. Carbonio, M. Hävecker, A. Knop-Gericke, R. Schloegl, M. F. Bekheet, A. Gurlo, A. Doran, J. Bernardi, B. Klötzer, S. Penner, *ECS Trans.* **2019**, 91, 1771.
- [57] D. N. Mueller, M. L. Machala, H. Bluhm, W. C. Chueh, *Nat. Commun.* **2015**, 6, 6097.
- [58] M. Abbate, F. M. F. de Groot, J. C. Fuggle, A. Fujimori, O. Strebler, F. Lopez, M. Domke, G. Kaindl, G. A. Sawatzky, M. Takano, Y. Takeda, H. Eisaki, S. Uchida, *Phys. Rev. B* **1992**, 46, 4511.
- [59] M. Kuhn, S. Hashimoto, K. Sato, K. Yashiro, J. Mizusaki, *Solid State Ionics* **2011**, 195, 7.
- [60] D. Marrocchelli, S. R. Bishop, H. L. Tuller, B. Yildiz, *Adv. Funct. Mater.* **2012**, 22, 1958.
- [61] F. Frati, M. O. J. Y. Hunault, F. M. F. de Groot, *Chem. Rev.* **2020**, 120, 4056.
- [62] T. Nakamura, R. Oike, Y. Ling, Y. Tamenori, K. Amezawa, *Phys. Chem. Chem. Phys.* **2016**, 18, 1564.
- [63] C. T. Chen, F. Sette, Y. Ma, M. S. Hybertsen, E. B. Stechel, W. M. C. Foulkes, M. Schuller, S.-W. Cheong, A. S. Cooper, L. W. Rupp Jr., B. Batlogg, Y. L. Soo, Z. H. Ming, A. Krol, Y. H. Kao, *Phys. Rev. Lett.* **1991**, 66, 104.
- [64] R. Thalinger, M. Gocyla, M. Heggen, B. Klötzer, S. Penner, *J. Phys. Chem. C* **2015**, 119, 22050.
- [65] J. S. Jeong, W. Wu, M. Topsakal, G. Yu, T. Sasagawa, M. Greven, K. Andre Mkhoyan, *Phys. Rev. Mater.* **2018**, 2, 054801.
- [66] D. Udomsilp, D. Roehrens, N. H. Menzler, C. Bischof, L. G. J. De Haart, A. K. Opitz, O. Guillon, M. Bram, *J. Electrochem. Soc.* **2017**, 164, F1375.
- [67] M. Chen, Y. Hu, D. Chen, H. Hu, Q. Xu, *Electrochim. Acta* **2018**, 284, 303.
- [68] A. K. Opitz, C. Rameshan, M. Kubicek, G. M. Rupp, A. Nanning, T. Götsch, R. Blume, M. Hävecker, A. Knop-Gericke, G. Rupprechter, B. Klötzer, J. Fleig, *Top. Catal.* **2018**, 61, 2129.
- [69] A. Nanning, A. K. Opitz, C. Rameshan, R. Rameshan, R. Blume, M. Hävecker, A. Knop-Gericke, G. Rupprechter, B. Klötzer, J. Fleig, *J. Phys. Chem. C* **2016**, 120, 1461.
- [70] E. J. Crumlin, E. Mutoro, W. T. Hong, M. D. Biegalski, H. M. Christen, Z. Liu, H. Bluhm, Y. Shao-Horn, *J. Phys. Chem. C* **2013**, 117, 16087.
- [71] N. Tsvetkov, Y. Chen, B. Yildiz, *J. Mater. Chem. A* **2014**, 2, 14690.
- [72] Y. Zhu, Z. He, Y. Choi, H. Chen, X. Li, B. Zhao, Y. Yu, H. Zhang, K. A. Stoerzinger, Z. Feng, Y. Chen, M. Liu, *Nat. Commun.* **2020**, 11, 4299.
- [73] A. Nanning, J. Fleig, *Surf. Sci.* **2019**, 680, 43.
- [74] S. Yu, D. Yoon, Y. Lee, H. Yoon, H. Han, N. Kim, C.-J. Kim, K. Ihm, T.-S. Oh, J. Son, *Nano Lett.* **2020**, 20, 3538.
- [75] A. K. Opitz, A. Nanning, S. Kogler, C. Rameshan, R. Rameshan, R. Blume, M. Hävecker, A. Knop-Gericke, G. Rupprechter, B. Klötzer, J. Fleig, *ECS Trans.* **2015**, 68, 3333.
- [76] A. K. Opitz, A. Nanning, C. Rameshan, R. Rameshan, R. Blume, M. Hävecker, A. Knop-Gericke, G. Rupprechter, J. Fleig, B. Klötzer, *Angew. Chem., Int. Ed.* **2015**, 54, 2628.
- [77] J. Zhou, Y. Chen, G. Chen, K. Wu, Y. Cheng, *J. Alloys Compd.* **2015**, 647, 778.
- [78] M. V. Patrakeeva, J. A. Bahteevaa, E. B. Mitberga, I. A. Leonidova, V. L. Kozhevnikova, K. R. Poepfelmeier, *J. Solid State Chem.* **2003**, 172, 219.
- [79] S. Kogler, A. Nanning, G. M. Rupp, A. K. Opitz, J. Fleig, *J. Electrochem. Soc.* **2015**, 162, F317.
- [80] J. B. Goodenough, *Phys. Rev.* **1955**, 100, 564.
- [81] Y. Shin, K.-Y. Doh, S. H. Kim, J. H. Lee, H. Bae, S.-J. Song, D. Lee, *J. Mater. Chem. A* **2020**, 8, 4784.
- [82] F. Chiabrera, I. Garbayo, D. Pla, M. Burriel, F. Wilhelm, A. Rogalev, M. Núñez, A. Morata, A. Tarancón, *APL Mater.* **2018**, 7, 013205.
- [83] Z. Hashin, S. Shtrikman, *J. Mech. Phys. Solids* **1963**, 11, 127.
- [84] S. H. Chang, S. K. Kim, Y.-M. Kim, Y. Dong, C. M. Folkman, D. W. Jeong, W. S. Choi, A. Y. Borisevich, J. A. Eastman, A. Bhattacharya, D. D. Fong, *APL Mater.* **2019**, 7, 071117.
- [85] K. K. Adepalli, J. Yang, J. Maier, H. L. Tuller, B. Yildiz, *Adv. Funct. Mater.* **2017**, 27, 1700243.
- [86] F. Chiabrera, I. Garbayo, L. López-Conesa, G. Martín, A. Ruiz-Cardad, M. Walls, L. Ruiz-González, A. Kordatos, M. Núñez, A. Morata, S. Estradé, A. Chronos, F. Peiró, A. Tarancón, *Adv. Mater.* **2019**, 31, 1805360.
- [87] U. Bauer, L. Yao, A. J. Tan, P. Agrawal, S. Emori, H. L. Tuller, S. Van Dijken, G. S. D. Beach, *Nat. Mater.* **2015**, 14, 174.
- [88] A. J. Tan, M. Huang, C. O. Avci, F. Büttner, M. Mann, W. Hu, C. Mazzoli, S. Wilkins, H. L. Tuller, G. S. D. Beach, *Nat. Mater.* **2019**, 18, 35.
- [89] C. Bi, Y. Liu, T. Newhouse-Ilige, M. Xu, M. Rosales, J. W. Freeland, O. Mryasov, S. Zhang, S. G. E. Te Velthuis, W. G. Wang, *Phys. Rev. Lett.* **2014**, 113, 267202.
- [90] V. B. Tinti, D. Marani, A. S. Ferlauto, F. C. Fonseca, V. Esposito, D. Z. Florio, *Part. Part. Syst. Character.* **2020**, 37, 1900472.
- [91] T. Pussacq, O. Menétré, F. Tessier, A. Löfberg, M. Huvé, J. Guerro Caballero, S. Colis, H. Kabbour, *J. Alloys Compd.* **2018**, 766, 987.
- [92] H. Matsuura, K. Seto, H. Yang, K. Kawano, M. Takahashi, T. Ogawa, *IEEE Trans. Magn.* **2008**, 44, 2804.
- [93] T.-J. Yoon, H. Shao, R. Weissleder, H. Lee, *Part. Part. Syst. Character.* **2013**, 30, 667.
- [94] F. Yang, X. Yang, Q. Lin, R. Wang, H. Yang, Y. He, *Mater. Sci.* **2019**, 25, 231.
- [95] J. Shi, B. T. Liu, Y. L. Jia, X. H. Li, X. H. Dai, D. Y. Ge, J. X. Guo, Y. J. Fu, Y. Zhou, L. Guan, Q. X. Zhao, J. Wang, X. Y. Zhang, L. X. Ma, *J. Alloys Compd.* **2016**, 663, 880.
- [96] Q. Li, C. W. Kartikowati, S. Horie, T. Ogi, T. Iwaki, K. Okuyama, *Sci. Rep.* **2017**, 7, 9894.

- [97] S. Ning, Q. Zhang, C. Occhialini, R. Comin, X. Zhong, C. A. Ross, *ACS Nano* **2020**, *14*, 8949.
- [98] J.-h Myung, D. Neagu, D. N. Miller, J. T. S. Irvine, *Nature* **2016**, *537*, 528.
- [99] Z. Chen, B. Hua, X. Zhang, L. Chen, Y.-Q. Zhang, G. Yang, G. Wang, H. Zhou, Y. Yang, J. Chen, H. Fan, Q. Li, M. Li, J. Li, W. Zhou, Z. Shao, J.-L. Luo, Y. Sun, *Cell Rep. Phys. Sci.* **2020**, *1*, 100243.

ADVANCED FUNCTIONAL MATERIALS

Supporting Information

for *Adv. Funct. Mater.*, DOI: 10.1002/adfm.202108005

Exsolution Synthesis of Nanocomposite Perovskites with
Tunable Electrical and Magnetic Properties

*Jiayue Wang, Komal Syed, Shuai Ning, Iradwikanari
Waluyo, Adrian Hunt, Ethan J. Crumlin, Alexander K.
Opitz, Caroline A. Ross, William J. Bowman, and Bilge
Yildiz**

Supporting Information

Exsolution synthesis of nanocomposite perovskites with tunable electrical and magnetic properties

Jiayue Wang¹, Komal Syed², Shuai Ning³, Iradwikanari Waluyo⁴, Adrian Hunt⁴, Ethan J. Crumlin⁵, Alexander K. Opitz⁶, Caroline A. Ross³, William Bowman², Bilge Yildiz^{1,3}*

¹Department of Nuclear Science and Engineering, Massachusetts Institute of Technology, Cambridge, MA, USA

²Department of Materials Science & Engineering, University of California, Irvine, CA USA

³Department of Materials Science and Engineering, Massachusetts Institute of Technology, Cambridge, MA, USA

⁴National Synchrotron Light Source II, Brookhaven National Laboratory, Upton, NY, USA

⁵Advanced Light Source, Lawrence Berkeley National Laboratory, Berkeley, CA, USA

⁶Institute of Chemical Technologies and Analytics, TU Wien, Vienna, Austria

* e-mail: byildiz@mit.edu

Supplementary Note 1: Complementary characterization of the LSF film

The as-prepared LSF surface contains a relatively flat background and protruding grains with an average size of ~ 30 nm (**Figure S1a**). Similar surface microstructures have also been observed in other PLD-grown perovskite thin films where relatively large lattice mismatch exists between the film and the substrate^{1,2}. After reducing the sample at 400 °C in 0.5 Torr flowing H₂, considerably smaller nanoparticles with a mean radius of ca. 8 nm appeared on the surface (**Figure S1b**).

Figure S2 displays the cross-sectional bright-field scanning transmission electron microscopy (BF-STEM) image of the as-prepared LSF film. As illustrated, conical nanostructures can be observed in the polycrystalline LSF film.

Figure S3 shows the out-of-plane X-ray diffraction (XRD) pattern of the LSF films before and after Fe⁰ exsolution. The as-prepared LSF film (**Figure S3a**) shows a clear (001) texture in the out-of-plane, with small components arising from (011). After Fe⁰ exsolution, no discernible α -Fe and Ruddlesden-Popper (La,Sr)₂FeO₄ reflections can be observed (**Figure S3b**). These findings indicate the (001)-oriented perovskite LSF remains to be the dominant phase (matrix) in the exsolved film. Meanwhile, the peak position for the LSF shifted to a lower 2θ position after Fe⁰ exsolution (**Figure S4**), which represents chemical expansion^{3,4} in the LSF lattice due to oxygen vacancy formation.

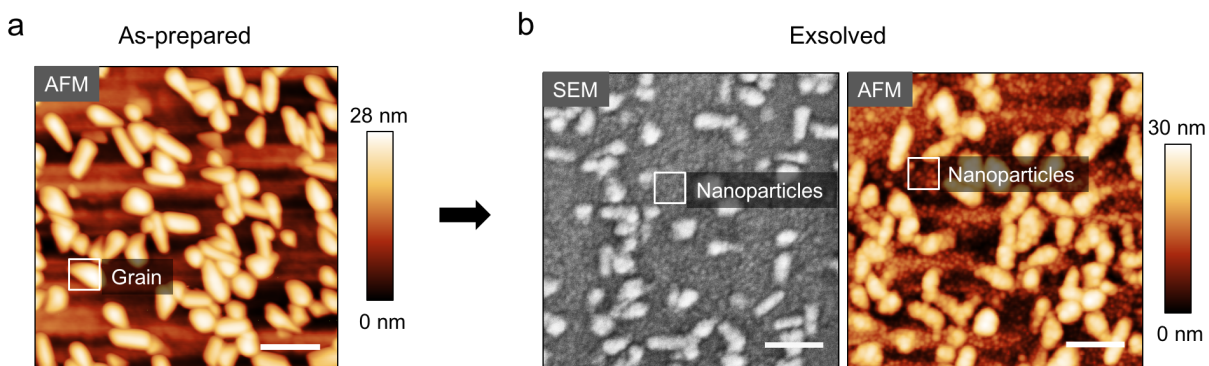


Figure S1. AFM and SEM image showing the surface morphology evolution (a) before and (b) after Fe exsolution. Notably, considerable nanoparticles appeared on the surface after Fe⁰ exsolution. The data were collected from the same sample. To reduce charging effect, the SEM image was collected with 10 nm carbon coating. Scale bars for all the images are 200 nm.

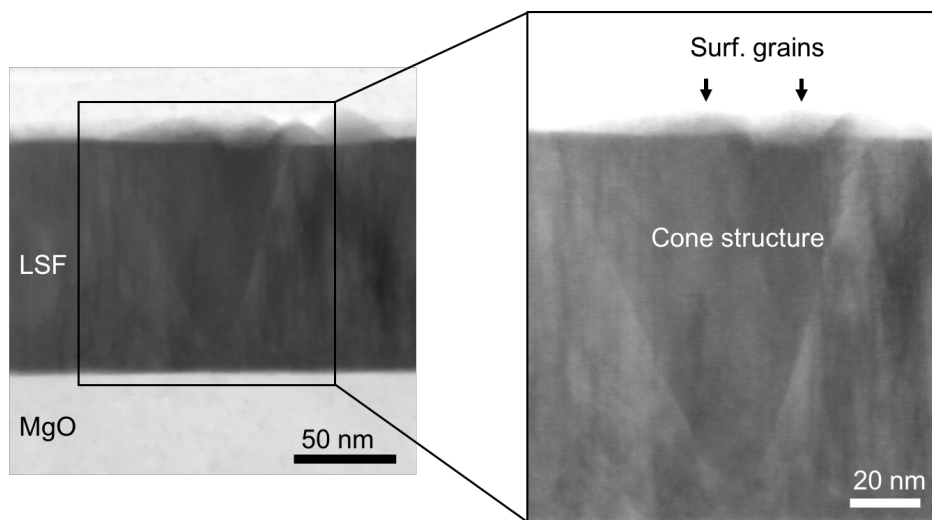


Figure S2. Cross-sectional BF-STEM image of the as-prepared LSF film grown on the MgO (001) substrate. Note the zoom-in plot highlights the conical nanopillar in the as-prepared LSF film. Note the surface grains observed by AFM (Figure 1 in the main text) can be also found here (indicated with arrows), which are located on top of the cone structure.

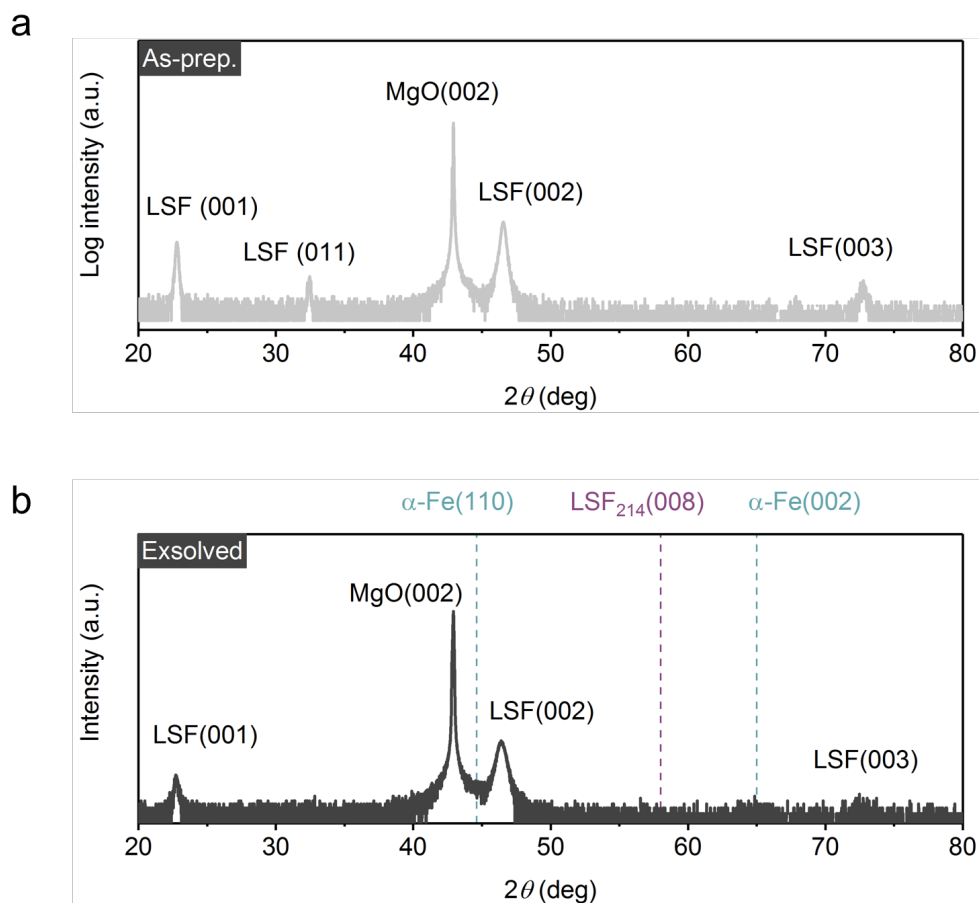


Figure S3. Out-of-plane symmetric 2θ - ω X-ray diffraction scan of the (a) as-prepared and (b) exsolved LSF thin films. The dotted lines in (b) indicate the peak positions of the BCC iron and the Ruddlesden-Popper phase LSF₂₁₄.

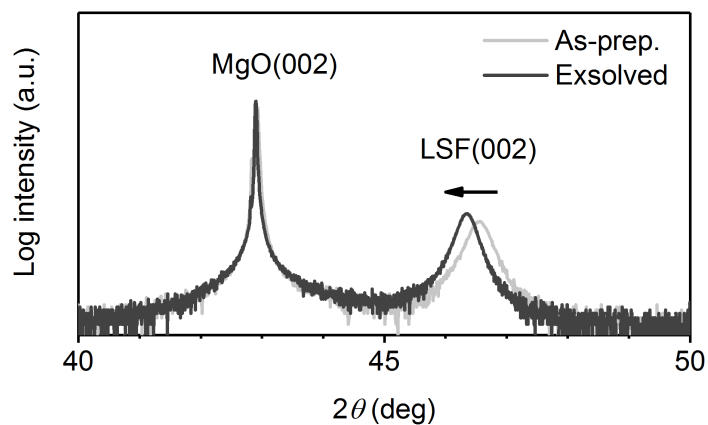


Figure S4. Out-of-plane symmetric 2θ - ω X-ray diffraction scans highlight the chemical expansion of the LSF lattice during Fe⁰ exsolution. The arrow indicates the peak shift direction of the LSF (002) reflection.

Supplementary Note 2: Percolating channels in the exsolved LSF film

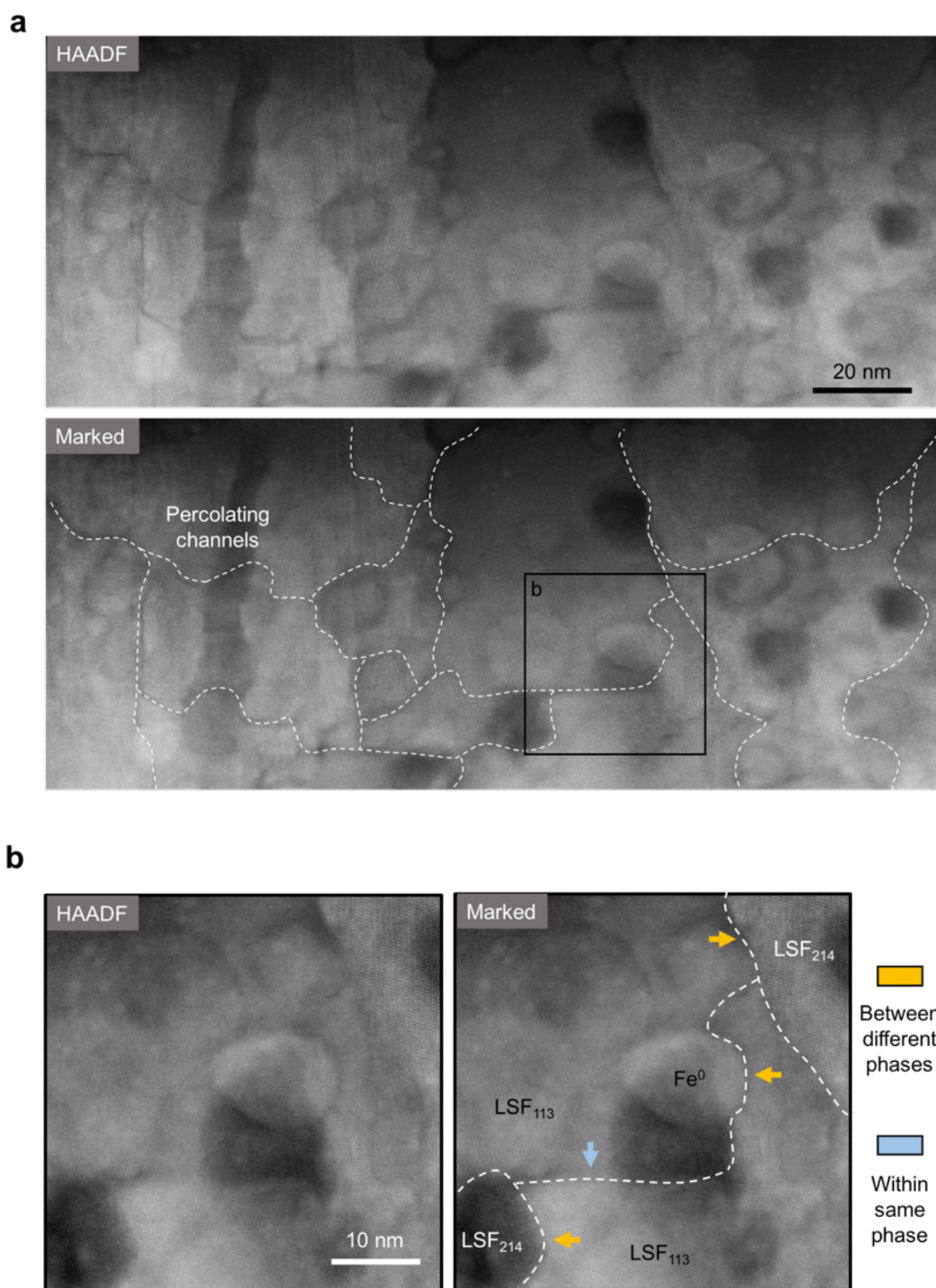


Figure S5. Percolating channels between the distinct phases as well as within the same phase. (a) Low magnification STEM high-angle annular dark field (HAADF) images showing the percolating channels in the exsolved LSF film. (b) Magnified HAADF images from the region highlighted in (a). The blue arrows highlight the percolating channels within the LSF₁₁₃ phase, while the yellow arrows show the channels at the phase boundaries between the matrix LSF₁₁₃, Ruddlesden-Popper phase LSF₂₁₄ and the metallic iron.

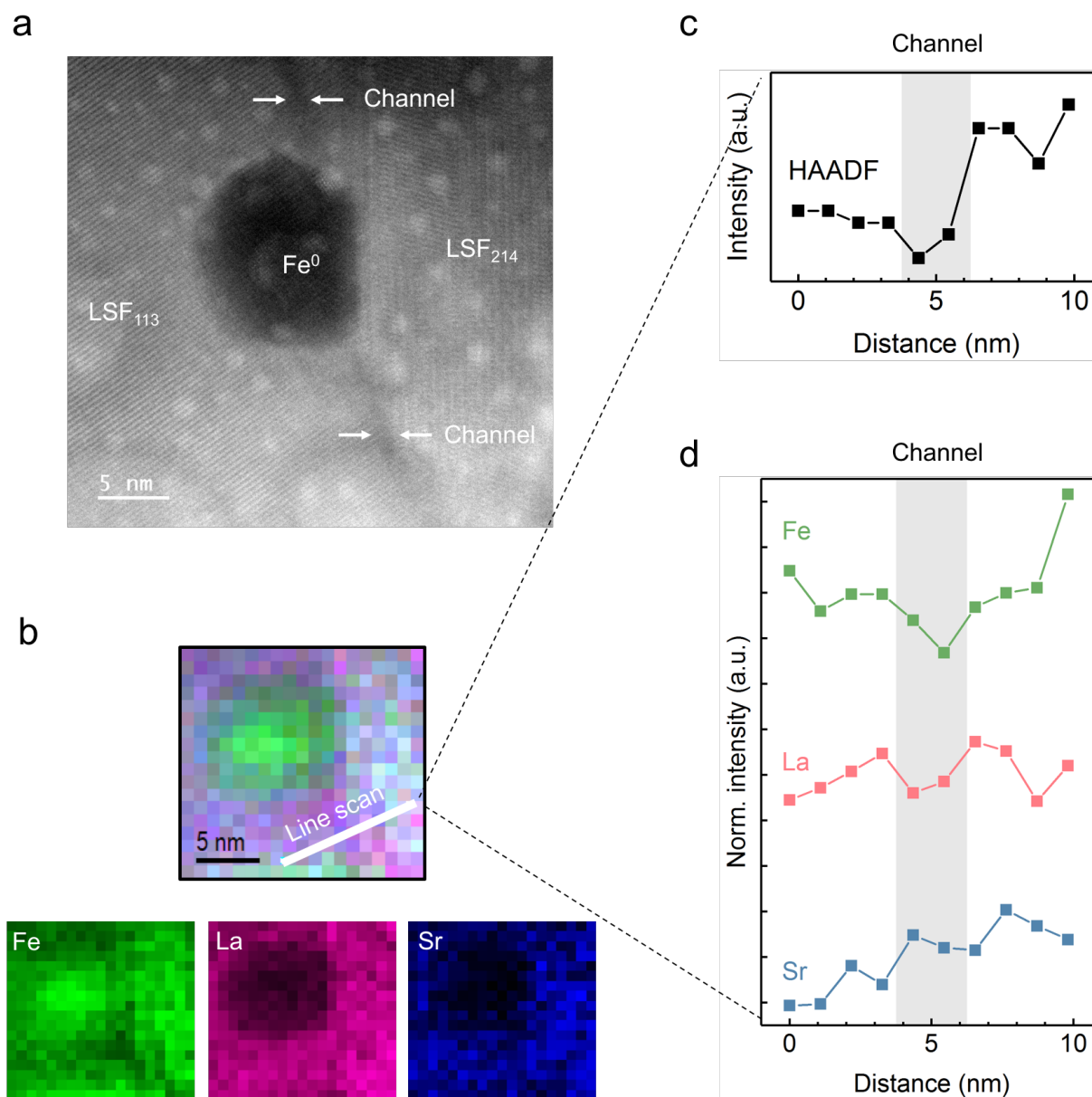


Figure S6. Chemical analysis of the percolating channel. (a) HAADF-STEM image showing bulk exsolved nanostructures. The percolating channels are indicated with arrows. (b) Composite image with overlap of Fe/La/Sr EDS counts map, together with the individual EDX mapping. The EDX mapping was conducted at the same location as in (a). Note the percolating channel correlates with the Fe depleted zone in the Fe-mapping. Line profiles showing variation in (c) HAADF intensity and the (d) normalized EDS elemental signal across the LSF_{113} - LSF_{214} phase boundary and the percolating channel. The location of the line scan is indicated by the white line in plot (b), and the channel regions are highlighted in grey in plot (c) and (d). Note the lowest point in HAADF intensity matches well with local minima in Fe-signal, suggesting that the percolating channels are Fe-deficient.

Supplementary Note 3: Additional EDX mapping

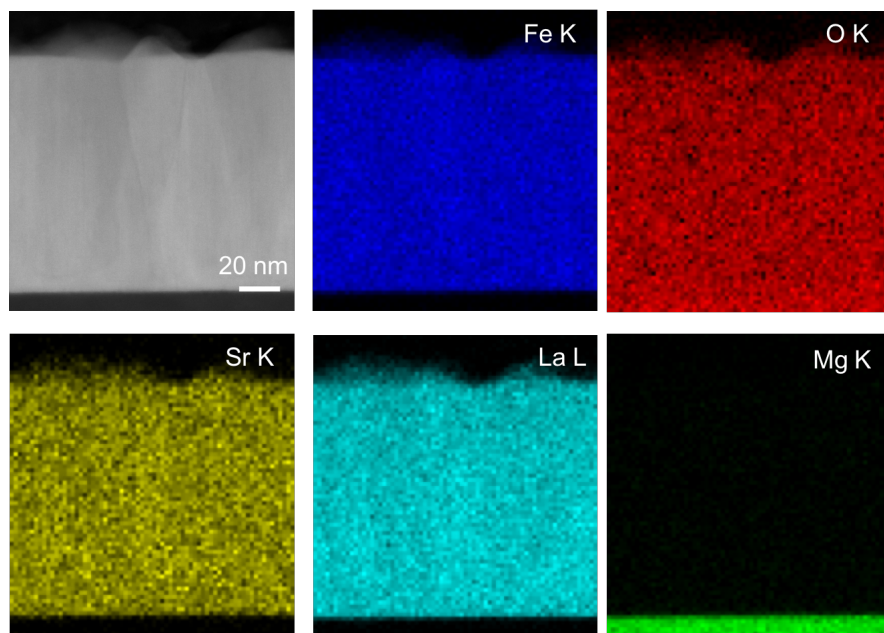


Figure S7. As-prepared LSF. HAADF imaging and the corresponding EDX chemical mapping showing the homogeneous bulk chemistry of the as-prepared LSF film.

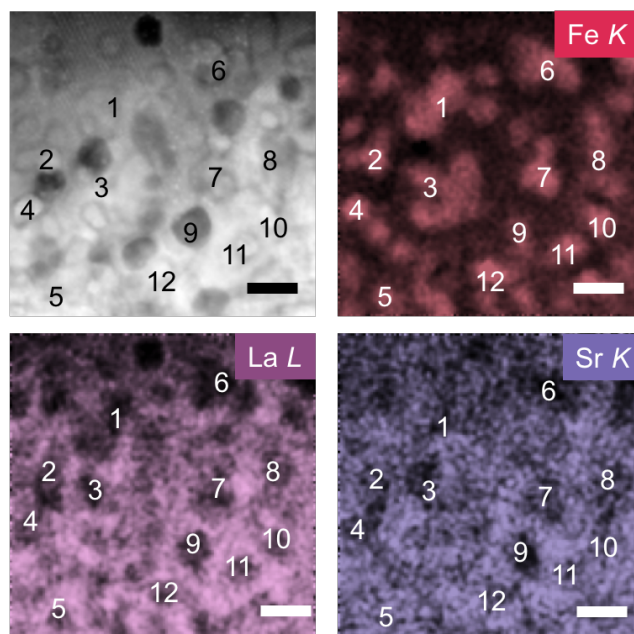


Figure S8. Exsolved LSF. HAADF imaging and the corresponding EDX chemical mapping showing the inhomogeneity in bulk chemistry of the LSF exsolved film. The numbers in each plot highlight some regions that are enriched in Fe while depleted in La and Sr. Scale bars: 10 nm.

Supplementary Note 4: Feature C in the O K-edge spectra

Here, we demonstrate that the feature C in the O K-edge are only present in LSF after Fe⁰ exsolution. To do so, we conducted *in-situ* partial electron yield X-ray absorption spectroscopy (PEY-XAS) on a mildly reduced LSF film, prior to Fe⁰ exsolution. As revealed by the O K-edge spectra in **Figure S9**, the pre-edge feature completely vanished after reducing the LSF film at 400 °C in 0.2 Torr H₂. The absence of the pre-edge feature indicates that the ligand hole concentration became negligible, indicating a considerable oxygen deficiency is present in LSF³. Nevertheless, feature C is not present in the O K-edge spectrum at this stage. These findings clearly indicate that the feature C is not from oxygen vacancies. We note the feature C agrees with the the La/Sr-O hybridization of La₂O₃⁵, SrO⁵, and Ruddlesden-Popper (RP) phase oxides⁶⁻⁸, which are all the likely decomposition products in exsolution⁹⁻¹².

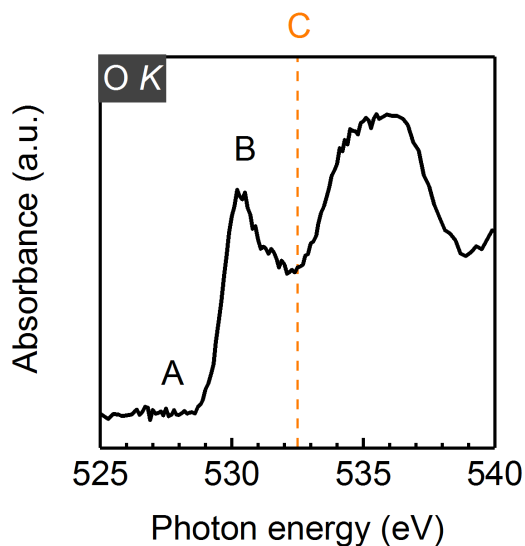


Figure S9. *In-situ* O K-edge PEY-XAS of the LSF film at 400 °C in 0.2 Torr H₂, without Fe⁰ exsolution. Note feature C is not present in the O K-edge XAS spectrum of the mildly reduced LSF film.

Supplementary Note 5: O* species in the O 1s spectra

First, we demonstrate that the O* species are only present in LSF after Fe⁰ exsolution. To do so, we conducted *in-situ* partial electron yield X-ray absorption spectroscopy (PEY-XAS) and NAP-XPS measurements on a mildly reduced LSF film, prior to Fe⁰ exsolution. As revealed by the O K-edge spectra in **Figure S10**, the pre-edge feature (i.e., the feature A) completely vanished after reducing the LSF film at 400 °C in 0.2 Torr H₂. The absence of the pre-edge feature suggests that the hole concentration became negligible, indicating a considerable oxygen deficiency is present in LSF³. Nevertheless, no O* peak is present in the O 1s spectrum at this stage. These findings clearly indicate that the O* species are not from lattice reduction (i.e., oxygen vacancy formation) alone.

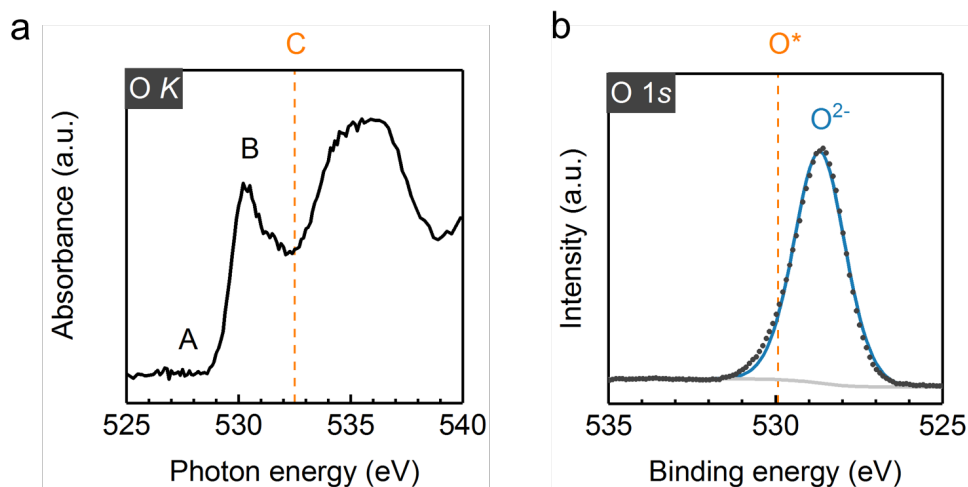
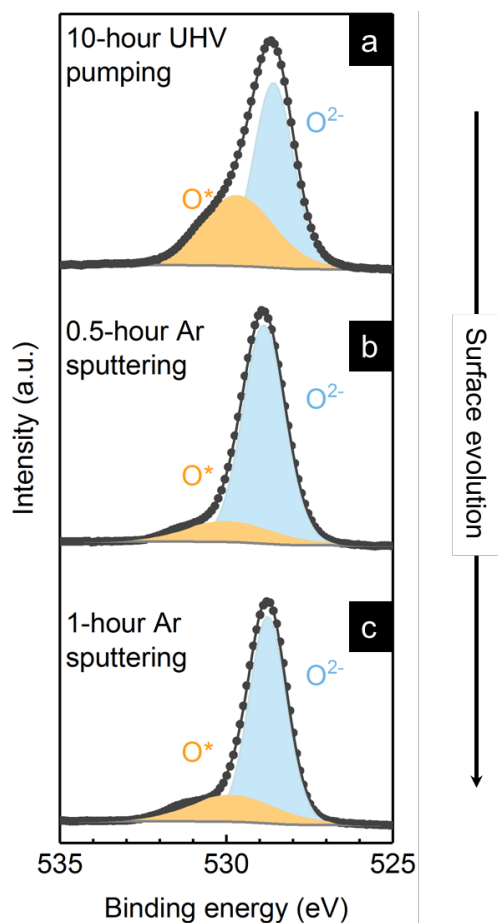


Figure S10. (a) O K-edge PEY-XAS and (b) O 1s XPS spectra of the LSF film at 400 °C in 0.2 Torr H₂, without Fe⁰ exsolution. Note no O* features is present in the O 1s spectrum. The O 1s spectrum is collected at a photo energy of 665 eV.

Second, we demonstrate that the O* species are not surface adsorbates. We first cool down the exsolved LSF film to room temperature and pump out the gas in the XPS chamber. After staying in the ultra-high vacuum (UHV) environment for 10 hours, we collected the O 1s spectrum on the

sample again, and the result is shown in **FigureS11a**. As illustrated, the O^* species are still present on the LSF surface after UHV pumping, indicating the O^* species are not likely to be surface adsorbates. To further demonstrate this idea, we collected the $O\ 1s$ upon 1 keV Ar^+ sputtering (10 mA emission current). As illustrated in **FigureS11b** and **FigureS11c**, the intensities of the O^* species decreased after half-hour Ar^+ sputtering, but remained almost invariant upon another half-hour sputtering. These findings indicate that while the surface has a higher concentration of O^* , there is still a considerable amount of O^* species in the sub-surfaces (or bulk lattice). Therefore, the O^* species are not likely to originate from the surface adsorbates either.



FigureS11. $O\ 1s$ spectra of the exsolved LSF film after a sequence of treatments: (a) pumping in UHV for 10 hours, (b) half-hour Ar sputtering, and (c) 1-hour Ar sputtering. The spectra are collected with a photon energy of 863 eV.

Supplementary Note 6: Defect chemistry and electrical conductivities of LSF

Here we summarize the bulk defect chemistry³ and electrical properties¹³ of LSF in **Figure S12**. At high pO_2 , LSF exhibit p -type conductivities with relatively low activation energies. In this region Sr doping is charge compensated by electron holes, and a characteristic +1/4 slope can clearly be observed in the conductivity- pO_2 plot (**Figure S12a**). As the sample gets reduced in the low pO_2 region, the conductivity decreased dramatically due to the depleted hole concentration. In this region, the ionic and electronic contributions to the total conductivity can be comparable. As a result, the electrical conductivity demonstrated large activation energy (~ 1.4 eV), which is similar to what we have observed for the reduced LSF (Figure 4b in the main text). Finally, at very reducing atmospheres, the LSF perovskite phase becomes unstable and starts to decompose (denoted as “Decomp.” in **Figure S12a**).

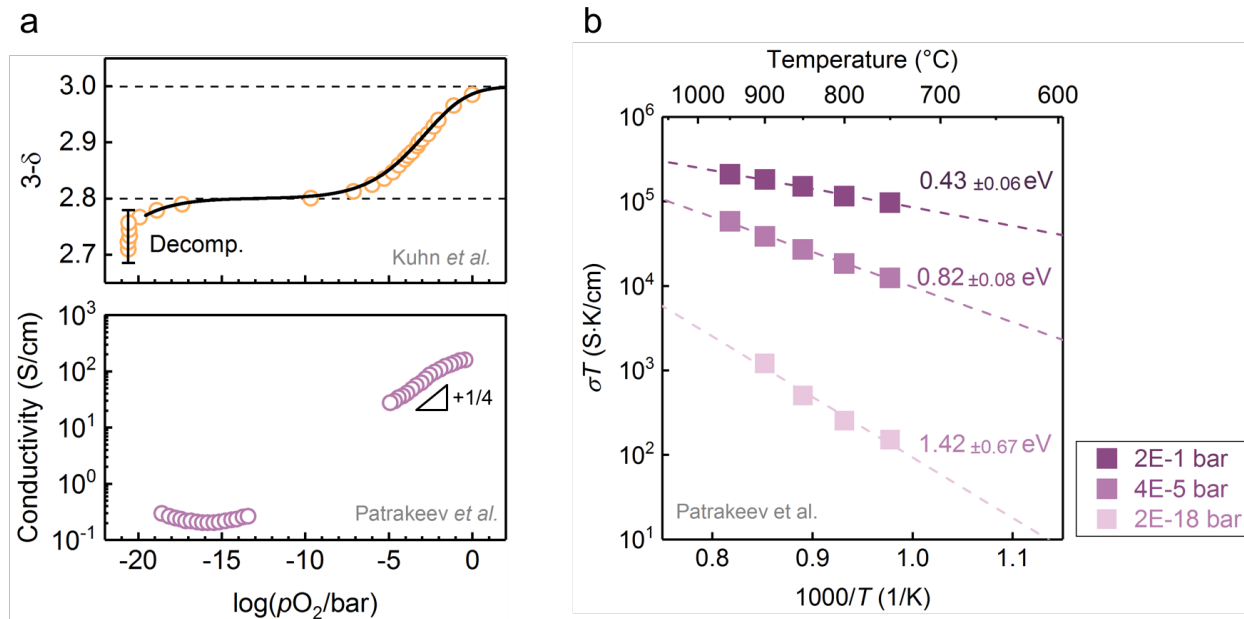


Figure S12. Bulk properties of the LSF from the literature. (a) Oxygen non-stoichiometry and electrical conductivity of powder $La_{0.6}Sr_{0.4}FeO_3$ (LSF) as a function of oxygen partial pressure (pO_2) at 800 °C. (b) Temperature-dependent electrical conductivities of powder LSF at different pO_2 . Figures are replotted with the data from ref. 3 and ref. 13.

Supplementary Note 7: Electrical conductivity measurement

During the two-probe measurement, the DC voltage was swept between -0.1 V and 0.1 eV between the two Pt current collectors. The resistances are calculated as the slope of the (ohmic) I-V curves using linear fitting and the conductivities are then calculated from the separation between the two Pt pads (5 mm) and the film thickness (110 nm).

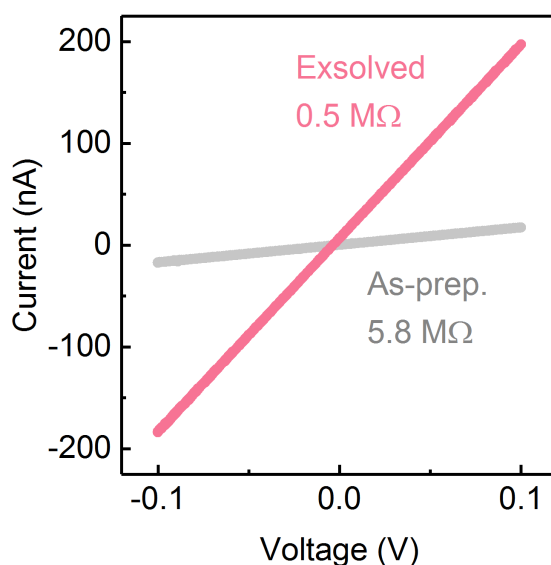


Figure S13. I-V curves of the as-prepared and exsolved LSF film in 0.5 Torr H₂ at 400 °C.

At low oxygen partial pressures, it is known from previous studies that the *n*-type electronic transport dominates the total electrical conductivity in LSF¹³ (see Supplementary Note 7). In this regime, the electronic transport occurs by small polaron conduction, which involves thermally activated hops of electron polarons (i.e., Fe²⁺)³. Therefore, the measured electrical conductivity in this work should be largely electronic. In accord with this assumption, impedance measurements at similar conditions also revealed negligible contributions from the ionic transport. As illustrated in **Figure S14**, only one high-frequency arc exists in the obtained impedance spectra. The absence of any low frequency electrode polarization resistance indicates the electrical conductance is

dominated by electronic transport^{14,15}. In addition, this high-frequency arc can be nicely fitted with one RICPE element, which represents the bulk resistance and the geometric capacitance (~ 0.1 nF) of the LSF thin film sample¹⁶.

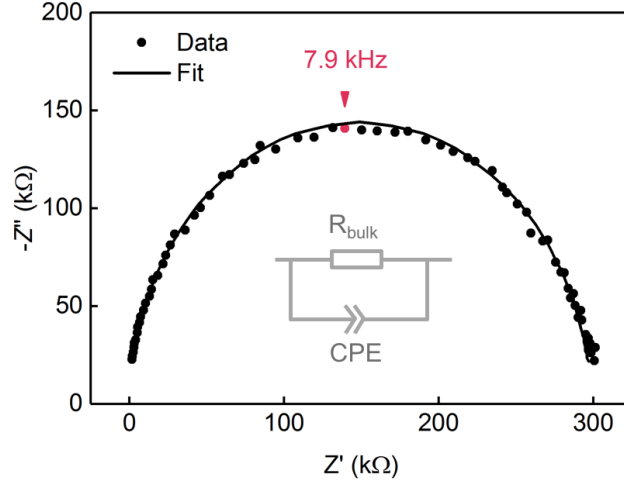


Figure S14. Impedance spectrum (circles) and fit (solid line) of an in-plane measurement of the LSF film at 600 °C in 200 sccm 5% H₂/N₂ atmosphere. The equivalent circuit consists of one RICPE element (CPE: constant phase element, $Z = 1/[Q(i\omega)^n]$). The fitting results are as follows: $R_{bulk} = 3.0 \times 10^5 \Omega$, $Q = 9.6 \times 10^{-11}$, $n = 9.7 \times 10^{-1}$. The geometric capacitance of the thin film can thus be calculated as¹⁷ $C = [Q \times R_{bulk}^{1-n}]^{1/n} = 7 \times 10^{-11}$ F. The fitting is performed using the ZView software.

As a result, the electrical conductivity (σ) of the LSF film can be expressed in terms of the elementary electron charge (e), and the concentration (c) and mobility (μ) of the charge carrier:

$$\sigma = c \cdot e \cdot \mu \quad (1)$$

The mobility μ , in the high-temperature adiabatic regime¹⁸, follows the Arrhenius behavior:

$$\mu = \frac{\mu_0}{T} \cdot \exp\left(-\frac{E}{k_B T}\right), \quad (2)$$

where E is the activation energy for electron migration and/or hopping, μ_0 is the pre-exponential factor, k_B is the Boltzmann constant, and T is the absolute temperature. Since the conductivity was measured in the cooling direction in H₂ atmosphere, we were able to freeze in the defect

chemistry of each sample during the measurement. The stable surface chemistry during the cooling process is exemplified by the *in-situ* NAP-XPS measurements (**Figure 3** and **Figure S15**). Since the specimens cannot change stoichiometry during cooling down in H₂, the charge carrier concentration (i.e., c in Eq. 1) stays constant during the electrical measurement. We can thus combine Eq. 1 and 2 into

$$\sigma T = c \cdot e \cdot \mu_0 \cdot \exp\left(-\frac{E}{k_B T}\right) \propto \exp\left(-\frac{E}{k_B T}\right). \quad (3)$$

As a result, the activation energy measured in the experiment originates mainly from the polaron migration, with negligible contributions from defect formation¹⁹.

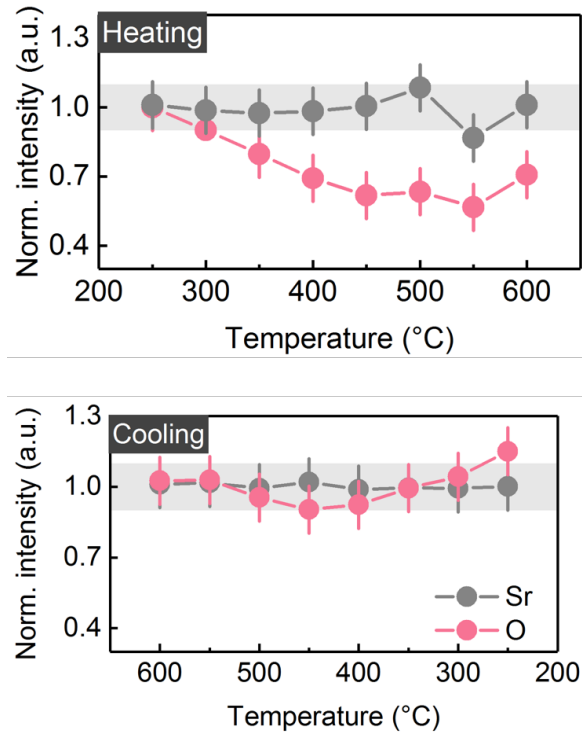


Figure S15. La 4d normalized Sr 3d and O 1s intensity of the LSF surface during (a) heating and (b) cooling in 0.5 Torr H₂. Note that the O intensity is almost stable during the cooling down process, indicating a stable oxygen non-stoichiometry. The horizontal gray band indicate the 10% uncertainty for the XPS analysis.

Since the thin-film samples have large resistances (on the orders of $M \Omega$, see **Figure S13**) due to the nanometer-scale thickness, we expect the contribution from the contact resistance to be minimal. To verify this, we compared the electrical conductivities measured by both 2-probe and 4-probe methods at 400 °C at around 0.2 Torr O_2 . The condition is selected because LSF at this condition represents the most conductive state (i.e., smallest resistance, see **Figure S22**). At this condition, the impact from the contact resistance should be the most obvious. The results are shown in the **Table S1** below, where the 2-probe measurement was conducted at the NAP-XPS beamline at NSLS-II, and the 4-probe measurement was conducted in the lab using Van der Pauw method. The Van der Pauw measurement was conducted on a 1 cm² LSF film grown MgO (001) substrate, using the same growth parameter as other samples in this work. To achieve ~0.2 Torr in the lab, an electrochemical O_2 pump was used. As shown in *Table S1*, the conductivities measured from the two measurements are similar ($\pm 2\%$). Therefore, we expect the contributions from the contact resistance to be minimum.

Table S1. Comparison between the electrical conductivities measured at 400 °C at around 0.2 Torr O_2 using 2-probe and 4-probe methods.

Pressure	Method	Conductivity (S/cm)
0.2 Torr	2-probe at synchrotron	37.88
0.14 Torr	4-probe in lab	38.65

Supplementary Note 8: Magnetic property of the exsolved Fe⁰ nanoparticles

The magnetic properties of bulk BCC Fe are listed in **Table S2**, where the values are taken from the Ref.²⁰. Since the exsolved LSF film has a saturation magnetization of $\sim 110 \text{ emu/cm}^3$ (see Figure 5e in the main text), we estimate the volume fraction of the iron nanoparticles in the nanocomposite LSF to be $\text{vol}\% = 110/1707 \times 100\% = 6.4\%$. Note this volume fraction is also close to the 2D area fraction of the nanoparticles in the STEM imaging ($\sim 8\%$, see **Figure S16**).

Table S2. Saturation magnetization of BCC iron at room temperature²⁰.

Materials	Magnetic structure	Saturation magnetization	Density	Saturation magnetization
α -Fe	Ferromagnetic	216 emu/g	7.9 g/cm ³	1707 emu/cm ³

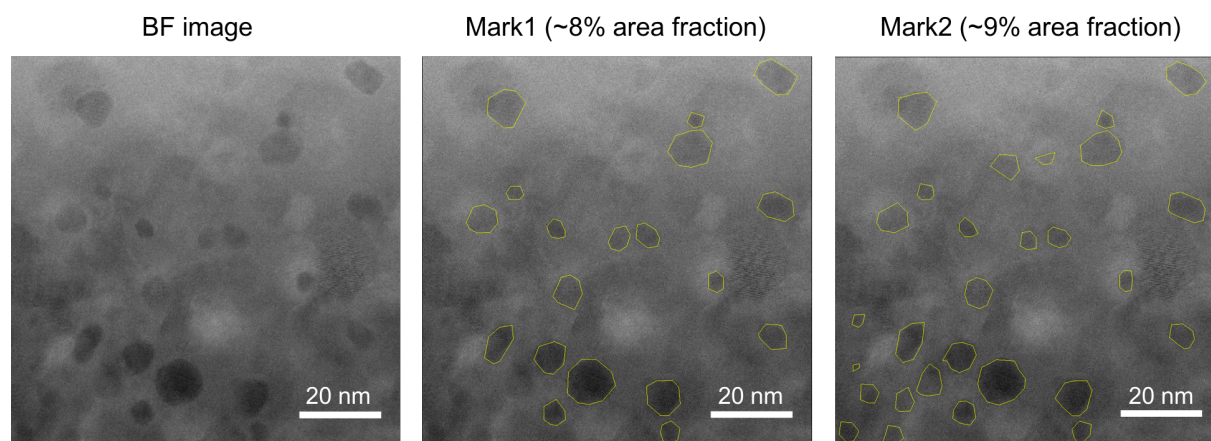


Figure S16. Bright field (BF) STEM images showing the exsolved nanoparticles in the bulk. In the BF imaging, the metallic nanoparticles have dark contrast. Due to the challenges to unambiguously identify every metallic nanoparticle, we employed two marking methods to estimate the area fraction of the nanoparticles in the STEM image. The area fraction from the two different markings are 8% and 9%, respectively. Note both values agree well with the Fe⁰ volume fraction estimated from the VSM.

The relationship between particle size and the magnetic properties (such as coercivity) of iron nanoparticles have been widely studied in the literature²¹. One crucial parameter determining the size-dependent magnetic property is the critical magnetic single-domain crystallite size, which depicts the transition from single-domain (SD) to multi-domain (MD) structures²². In the SD region, coercivity decreases with particle size until reaching the superparamagnetic limit²³. For the exsolved Fe⁰ particles in this study, their geometries were quantified with cross-sectional TEM. As a result, the axial ratio (i.e., the ratio of major axis length to minor axis) was calculated to be 0.7 ± 0.2 , while the particle size to be 12.1 ± 4.8 nm. By comparing the particle geometry with the theoretical phase diagram²⁴ of metallic iron (**Figure S17**), we can clearly tell that the nanoparticles are in the single-domain (SD) region.

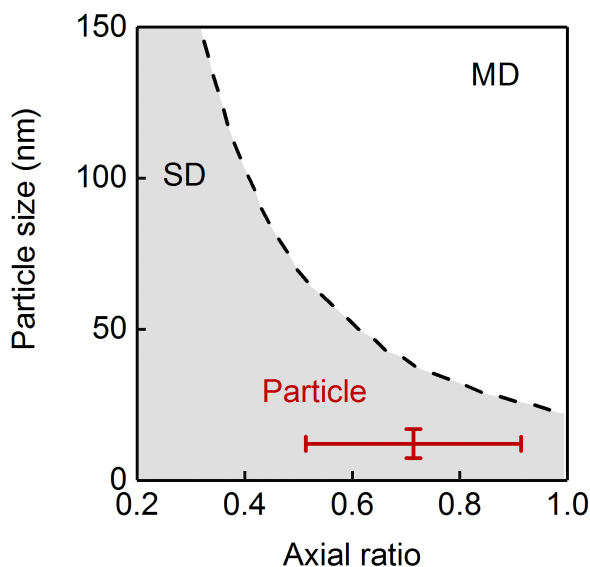


Figure S17. Phase diagram showing the stable single-domain (SD) region of the metallic iron, as a function of particle size and axial ratio (i.e., short-axis/long-axis ratio). The dashed line is the theoretical boundary between the SD and multi-domain (MD) structures for metallic iron, replotted from ref. ²⁴. The particle geometry is calculated from the cross-sectional TEM images of the nanocomposite LSF. Error bars are calculated based on 30 nanoparticles. Note the exsolved Fe⁰ nanoparticles are expected to adopt the SD state.

Supplementary Note 9: Finite element analysis

As shown in **Figure S18**, the percolating channels that are perpendicular to the electrical currents have negligible contributions to the total electrical conductivity.

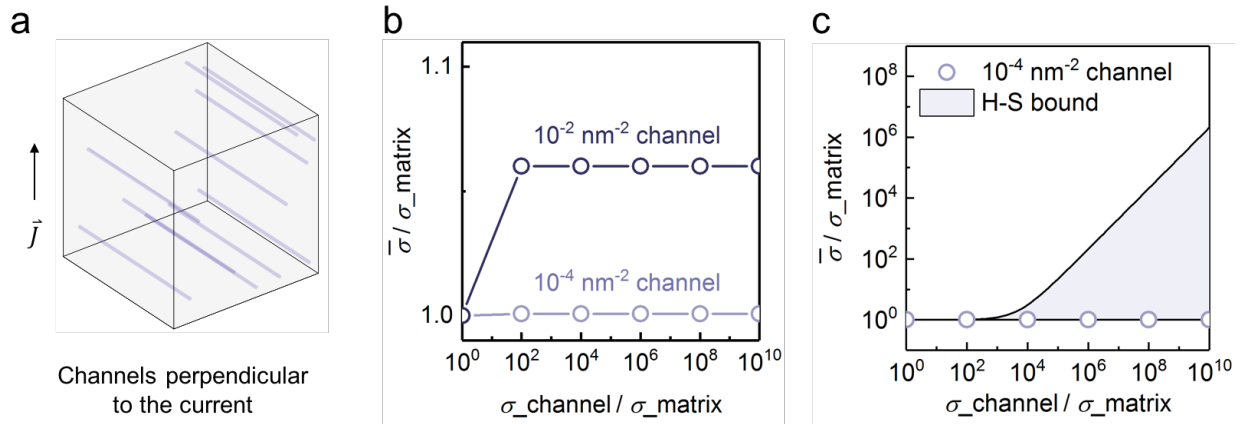


Figure S18. Impact of perpendicular channels to the electrical conductivity. (a) Finite element analysis (FEA) models of the percolating channels that are perpendicular to the electrical current. (b) Total electrical conductivity of the nanocomposite as a function of channel density. (c) Comparison of the finite element calculation to the Hashin–Shtrikman (H-S) bounds.

Supplementary Note 10: Redox cycling experiment

The exsolved LSF film was exposed to a cyclic gas change between 0.2 Torr O₂ and 0.5 Torr H₂ at 400 °C, where each cycle lasted around 2 hours. The gas composition in the main chamber during was monitored with mass spectrometry (MS) and is shown in **Figure S19**.

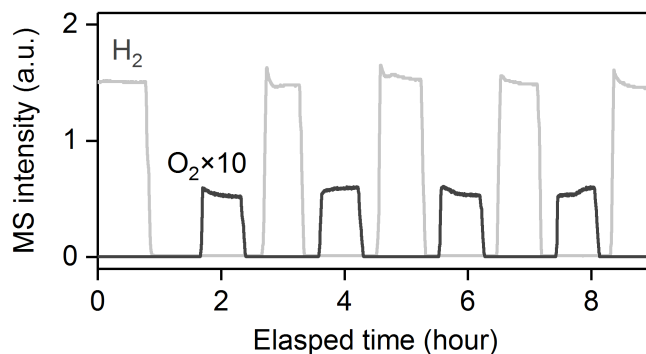


Figure S19. Mass spectrometry (MS) showing the gas composition in the reaction chamber during the redox cycling between 0.2 Torr O₂ and 0.5 Torr H₂ at 400 °C. The O₂ signal is magnified by 10 for visibility.

Typical surface morphologies of the LSF films during exsolution and re-oxidation are summarized in **Figure S20**. As illustrated, the nanoparticles did not reintegrate into the host oxide upon re-oxidation. The *ex-situ* AFM imaging and the *in-situ* NAP-XPS measurements (Figure 5) confirm that the oxidation process did not dissolve the Fe⁰ nanoparticles, but oxidized them into iron oxides.

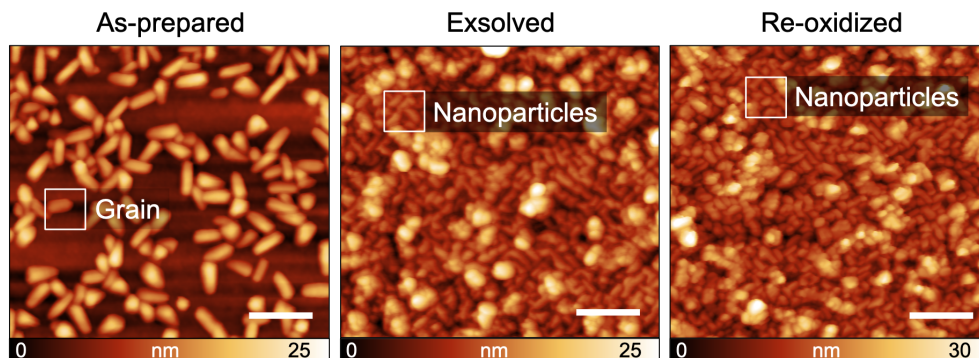


Figure S20. *Ex-situ* AFM images showing the surface morphology evolution during exsolution and re-oxidation. Scale bars: 200 nm. The exsolution condition is 5-hour annealing in 200 sccm 5% H₂/N₂ at 700 °C. The re-oxidation condition is 2-hour annealing in static air at 400 °C. Note the re-oxidation process did not dissolve the exsolved nanoparticles.

As shown in **Figure S21**, the thin-film conductivity decreased after each oxidation treatment and increased upon the successive re-reduction. Unlike the highly reversible surface chemistry, the bulk electrical conductivity varied in a seemingly damped fashion during the redox cycling. As a result, the electrical conductivity converged asymptotically to ~ 0.5 S/cm after four redox cycles. This irreversible redox behavior may be caused by the microstrains²⁵ accumulated in the nanocomposite LSF during the redox cycling.

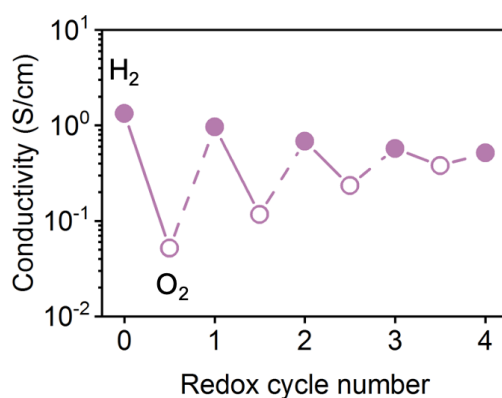


Figure S21. In-plane electrical conductivity of the exsolved LSF film during redox cycling between 0. The solid and dashed lines indicate the oxidation and reduction step, respectively. Here, cycle 0 represents the as-exsolved state. The cycling condition is 0.2 Torr O₂ and 0.5 Torr H₂ at 400 °C. Note that the conductivity of the nanocomposite LSF decreased after re-oxidation.

To compare the materials properties of the nanocomposite LSF (during the fourth redox cycle) and that of the as-prepared state, we summarized the surface chemistry and electrical conductivity of these two samples in **Figure S22**. The electrical conductivities of the nanocomposite LSF in the oxidizing condition (400 °C, 0.2 Torr O₂) is worth further discussion. As shown in **Figure S22**, the as-prepared perovskite LSF film has a conductivity as high as ~ 40 S/cm at the same condition. The low electrical conductivity of the nanocomposite LSF thus clearly indicates the re-oxidation step did not transform the thin film back to its as-prepared state (i.e., the single-phase perovskite) under the current experiment condition.

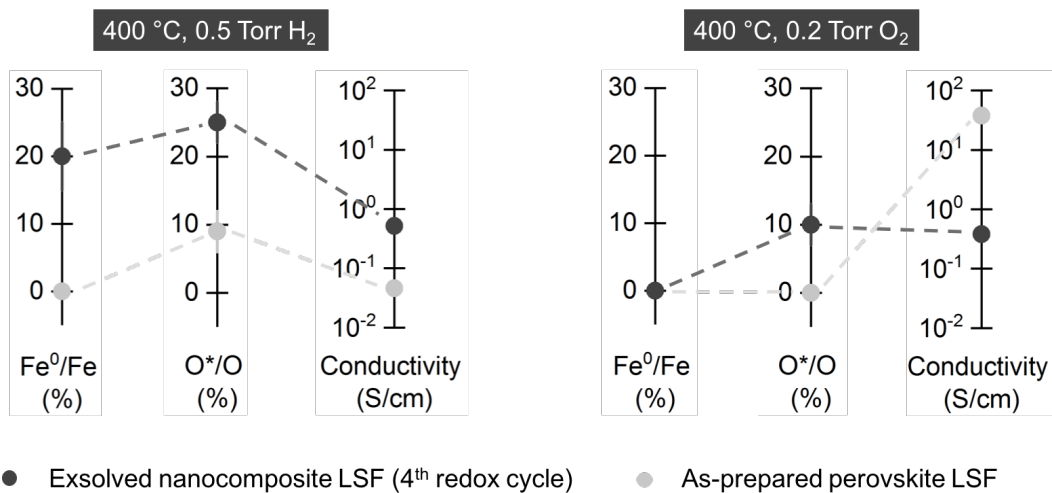


Figure S22. Comparison of the surface chemistry and electrical conductivity in the reducing (400 °C, 0.5 Torr H₂) and oxidizing (400 °C, 0.2 Torr O₂) atmospheres between the as-prepared LSF and the Fe⁰ exsolved LSF in the 4th redox cycle. EC stands for electrical conductivity and it is shown on a log scale. The dashed lines are the guide to the eye.

Supplementary Note 11: Magnetic properties of the LSF film

As the single crystal MgO substrate is diamagnetic at room temperature²⁶, we extract the LSF film contribution in the M - H loop with linear background subtraction (**Figure S23**).

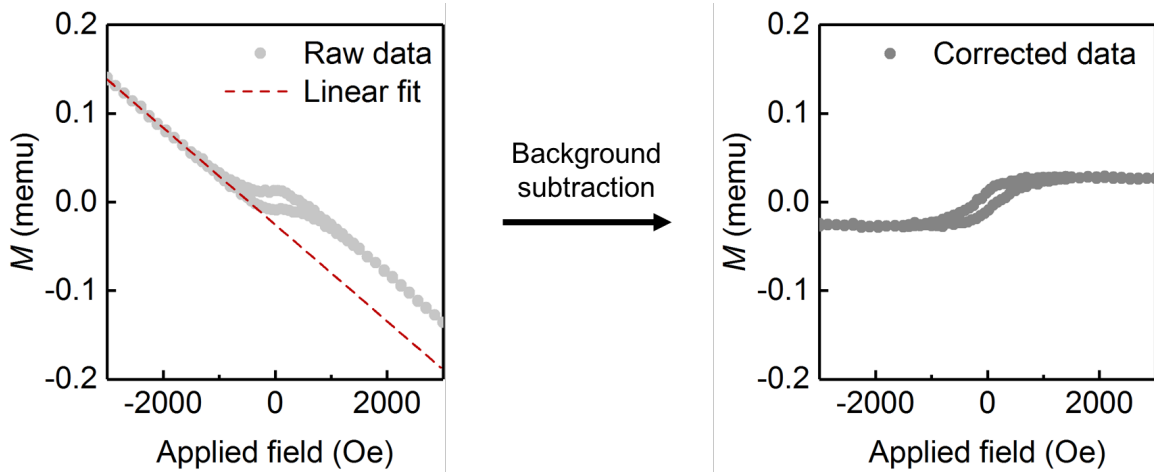


Figure S23. Background subtraction procedure for the VSM measurement.

As shown in **Figure S24**, the reduced LSF film (prior to exsolution) has a weaker magnetic property than the as-prepared LSF film. This indicates the strong magnetization after Fe^0 exsolution is from the nanoparticles instead of the perovskite matrix. After exsolution, the saturation magnetization increased considerably. In addition, as revealed by the similar in-plane and out-of-plane M - H loops (**Figure S25**), the magnetic property of the exsolved LSF film is isotropic. The isotropic magnetic properties agree with the isotropic particle geometries revealed by STEM imaging.

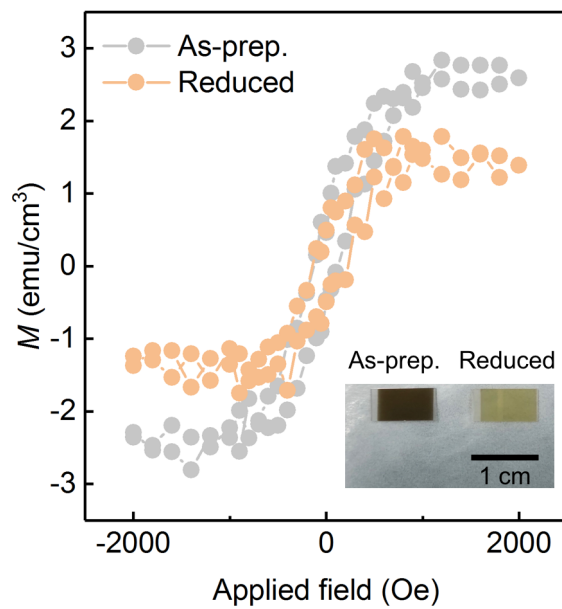


Figure S24. *Ex-situ* room temperature M - H loops of the as-prepared LSF and the reduced LSF film. Inset: optical images of the LSF films at these two states.

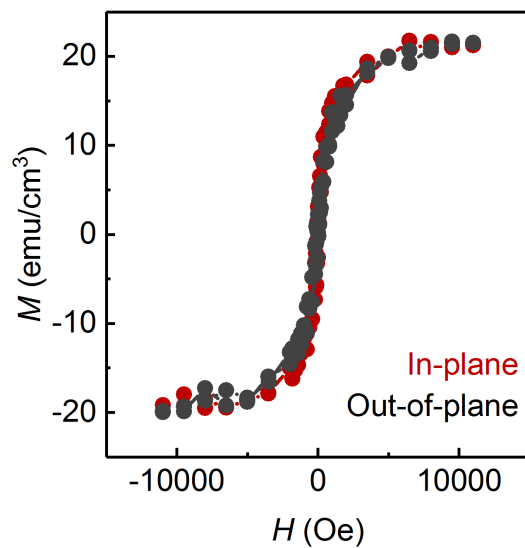


Figure S25. Comparison of the in-plane and out-of-plane M - H loops of the exsolved LSF film.

References

- 1 Tang, A. S., Onbasli, M. C., Sun, X. & Ross, C. A. Thickness-Dependent Double-Epitaxial Growth in Strained SrTi_{0.7}Co_{0.3}O_{3-δ} Films. *ACS Applied Materials & Interfaces* **10**, 7469-7475, doi:10.1021/acsami.7b18808 (2018).
- 2 Kim, H.-S. *et al.* Self-Assembled Single-Phase Perovskite Nanocomposite Thin Films. *Nano Letters* **10**, 597-602, doi:10.1021/nl903611t (2010).
- 3 Kuhn, M., Hashimoto, S., Sato, K., Yashiro, K. & Mizusaki, J. Oxygen nonstoichiometry, thermo-chemical stability and lattice expansion of La_{0.6}Sr_{0.4}FeO_{3-δ}. *Solid State Ionics* **195**, 7-15, doi:<https://doi.org/10.1016/j.ssi.2011.05.013> (2011).
- 4 Marrocchelli, D., Bishop, S. R., Tuller, H. L. & Yildiz, B. Understanding Chemical Expansion in Non-Stoichiometric Oxides: Ceria and Zirconia Case Studies. *Advanced Functional Materials* **22**, 1958-1965, doi:<https://doi.org/10.1002/adfm.201102648> (2012).
- 5 Frati, F., Hunault, M. O. J. Y. & de Groot, F. M. F. Oxygen K-edge X-ray Absorption Spectra. *Chemical Reviews* **120**, 4056-4110, doi:10.1021/acs.chemrev.9b00439 (2020).
- 6 Nakamura, T., Oike, R., Ling, Y., Tamenori, Y. & Amezawa, K. The determining factor for interstitial oxygen formation in Ruddlesden–Popper type La₂NiO₄-based oxides. *Physical Chemistry Chemical Physics* **18**, 1564-1569, doi:10.1039/C5CP05993C (2016).
- 7 Li, J. *et al.* Topotactic phase transformations by concerted dual-ion migration of B-site cation and oxygen in multivalent cobaltite La–Sr–Co–Ox films. *Nano Energy*, 105215, doi:<https://doi.org/10.1016/j.nanoen.2020.105215> (2020).
- 8 Chen, C. T. *et al.* Electronic states in La_{2-x}Sr_xCuO₄ probed by soft-x-ray absorption. *Physical Review Letters* **66**, 104-107, doi:10.1103/PhysRevLett.66.104 (1991).
- 9 Thalinger, R., Gocyla, M., Heggen, M., Klötzer, B. & Penner, S. Exsolution of Fe and SrO Nanorods and Nanoparticles from Lanthanum Strontium Ferrite La_{0.6}Sr_{0.4}FeO_{3-δ} Materials by Hydrogen Reduction. *The Journal of Physical Chemistry C* **119**, 22050-22056, doi:10.1021/acs.jpcc.5b06014 (2015).
- 10 Jeong, J. S. *et al.* Decomposition of La_{2-x}Sr_xCuO₄ into several La₂O₃ phases at elevated temperatures in ultrahigh vacuum inside a transmission electron microscope. *Physical Review Materials* **2**, 054801, doi:10.1103/PhysRevMaterials.2.054801 (2018).
- 11 Udomsilp, D. *et al.* High-Performance Metal-Supported Solid Oxide Fuel Cells by Advanced Cathode Processing. *Journal of The Electrochemical Society* **164**, F1375-F1384, doi:10.1149/2.0571713jes (2017).
- 12 Nishihata, Y. *et al.* Self-regeneration of a Pd-perovskite catalyst for automotive emissions control. *Nature* **418**, 164-167, doi:10.1038/nature00893 (2002).
- 13 Patrakeev, M. V. *et al.* Electron/hole and ion transport in La_{1-x}Sr_xFeO_{3-δ}. *Journal of Solid State Chemistry* **172**, 219-231, doi:[https://doi.org/10.1016/S0022-4596\(03\)00040-9](https://doi.org/10.1016/S0022-4596(03)00040-9) (2003).
- 14 Nenning, A. *et al.* The Electrochemical Properties of Sr(Ti,Fe)O_{3-δ} for Anodes in Solid Oxide Fuel Cells. *Journal of The Electrochemical Society* **164**, F364-F371, doi:10.1149/2.1271704jes (2017).
- 15 Adepalli, K. K., Yang, J., Maier, J., Tuller, H. L. & Yildiz, B. Tunable Oxygen Diffusion and Electronic Conduction in SrTiO₃ by Dislocation-Induced Space Charge Fields. *Advanced Functional Materials* **27**, 1700243, doi:10.1002/adfm.201700243 (2017).

- 16 Viernstein, A. *et al.* High-Temperature Photochromism of Fe-Doped SrTiO₃ Caused by UV-Induced Bulk Stoichiometry Changes. *Advanced Functional Materials* **29**, 1900196, doi:10.1002/adfm.201900196 (2019).
- 17 Fleig, J. The grain boundary impedance of random microstructures: numerical simulations and implications for the analysis of experimental data. *Solid State Ionics* **150**, 181-193, doi:[https://doi.org/10.1016/S0167-2738\(02\)00274-6](https://doi.org/10.1016/S0167-2738(02)00274-6) (2002).
- 18 Rettie, A. J. E., Chemelewski, W. D., Emin, D. & Mullins, C. B. Unravelling Small-Polaron Transport in Metal Oxide Photoelectrodes. *The Journal of Physical Chemistry Letters* **7**, 471-479, doi:10.1021/acs.jpcclett.5b02143 (2016).
- 19 Chen, D., Cao, Y., Weng, D. & Tuller, H. L. Defect and Transport Model of Ceria-Zirconia Solid Solutions: Ce_{0.8}Zr_{0.2}O_{2-δ}—An Electrical Conductivity Study. *Chemistry of Materials* **26**, 5143-5150, doi:10.1021/cm502565b (2014).
- 20 O'handley, R. C. *Modern magnetic materials: principles and applications*. (Wiley, 2000).
- 21 Sivaranjani, K. S., Antilen Jacob, G. & Justin Joseyphus, R. Coercivity and exchange bias in size reduced iron obtained through chemical reduction. *Journal of Magnetism and Magnetic Materials* **513**, 167228, doi:<https://doi.org/10.1016/j.jmmm.2020.167228> (2020).
- 22 Li, Q. *et al.* Correlation between particle size/domain structure and magnetic properties of highly crystalline Fe₃O₄ nanoparticles. *Scientific Reports* **7**, 9894, doi:10.1038/s41598-017-09897-5 (2017).
- 23 Andersen, H. L. & Christensen, M. In situ powder X-ray diffraction study of magnetic CoFe₂O₄ nanocrystallite synthesis. *Nanoscale* **7**, 3481-3490, doi:10.1039/C4NR06937D (2015).
- 24 Muxworthy, A. R. & Williams, W. Critical single-domain grain sizes in elongated iron particles: implications for meteoritic and lunar magnetism. *Geophysical Journal International* **202**, 578-583, doi:10.1093/gji/ggv180 (2015).
- 25 Kousi, K., Neagu, D., Bekris, L., Papaioannou, E. I. & Metcalfe, I. S. Endogenous Nanoparticles Strain Perovskite Host Lattice Providing Oxygen Capacity and Driving Oxygen Exchange and CH₄ Conversion to Syngas. *Angewandte Chemie International Edition* **59**, 2510-2519, doi:10.1002/anie.201915140 (2020).
- 26 Cao, M. *et al.* Point defects and magnetic properties of neutron irradiated MgO single crystal. *AIP Advances* **7**, 056413, doi:10.1063/1.4973942 (2017).